

Mixing of materials in magnetised core-collapse supernova remnants

D. M.-A. Meyer^{★1}, M. Pohl^{1,2}, M. Petrov³ and K. Egberts¹

¹ Universität Potsdam, Institut für Physik und Astronomie, Karl-Liebknecht-Strasse 24/25, 14476 Potsdam, Germany

² Deutsches Elektronen-Synchrotron (DESY), Platanenallee 6, 15738 Zeuthen, Germany

³ Max Planck Computing and Data Facility (MPCDF), Gießenbachstrasse 2, D-85748 Garching, Germany

Last updated 2020 June 10; in original form 2013 September 5

ABSTRACT

Core-collapse supernova remnants are structures of the interstellar medium (ISM) left behind the explosive death of most massive stars ($\lesssim 40 M_{\odot}$). Since they result in the expansion of the supernova shock wave into the gaseous environment shaped by the star’s wind history, their morphology constitutes an insight into the past evolution of their progenitor star. Particularly, fast-moving massive stars can produce asymmetric core-collapse supernova remnants. We investigate the mixing of materials in core-collapse supernova remnants generated by a moving massive $35 M_{\odot}$ star, in a magnetised ISM. Stellar rotation and the wind magnetic field are time-dependently included into the models which follow the entire evolution of the stellar surroundings from the zero-age main-sequence to 80 kyr after the supernova explosion. It is found that very little main-sequence material is present in remnants from moving stars, that the Wolf-Rayet wind mixes very efficiently within the 10 kyr after the explosion, while the red supergiant material is still unmixed by 30% within 50 kyr after the supernova. Our results indicate that the faster the stellar motion, the more complex the internal organisation of the supernova remnant and the more effective the mixing of ejecta therein. In contrast, the mixing of stellar wind material is only weakly affected by progenitor motion, if at all.

Key words: MHD – stars: evolution – stars: massive – ISM: supernova remnants.

1 INTRODUCTION

High-mass stars are defined as stellar objects of mass M_{\star} heavier than $8 M_{\odot}$ (Salpeter 1955; Kroupa 2001), and they represent $\approx 1\%$ of all stars in the Milky Way. They form in dense and highly opaque giant molecular clouds, as a result of the local free-fall gravitational collapse of dense cold gas (Shu 1992). They follow a formation scenario that is a scaled-up version of that of low-mass stars (Vorobyov & Basu 2006; Vorobyov 2009, 2010), and which is well-described by the so-called burst mode of accretion in star formation (Meyer et al. 2017, 2021a). When the infalling molecular material lands onto a centrifugally-balanced accretion disc, it undergoes gravitational instability and gaseous clumps can form and inward-migrate onto stellar surface, adding mass to the young massive star (Meyer et al. 2019). Once massive protostars are hot enough, their ionizing feedback dissipate their surrounding molecular environment and they release strong supersonic winds from the stellar surface (Vink et al. 2000) to interact directly with the interstellar medium (ISM), giving birth to stellar wind bubbles (Weaver et al. 1977).

As a function of multiplicity (Sana et al. 2012), metallicity (Brott et al. 2011a,b) and rotation properties (Maeder & Meynet 2000; Szécsi et al. 2022), massive stars evolve from a long initial main-sequence phase by undergoing several evolutionary phases, characterised by abrupt surface properties changes, alternating between hot, fast-winded with cold, slow-winded phases (Langer 2012). Although exotic evolutionary phases exist (Smith 2014; Groh

et al. 2014), a high-mass star typically goes through a red supergiant phase (Levesque 2010; Davies 2017), followed, in the case $M_{\star} \geq 30 M_{\odot}$, by a Wolf-Rayet phase (Underhill 1968; Hamann 1992; Crowther 2007), before exploding as a supernova (Woosley & Weaver 1986; Weiler & Sramek 1988; Smartt 2009). The circumstellar medium of massive stars is the region of the ISM directly surrounding high-mass stellar objects and it adopts morphologies and emission properties reflecting both the stellar feedback and the ambient medium properties.

The surroundings of young massive stellar objects are massive accretion discs of radius ~ 1000 au (Johnston et al. 2015; Ilee et al. 2016; Ahmadi et al. 2018) that are evaporated and blown by the radiation field and the wind of zero-age main-sequence high-mass stars. Their environments adopt the theoretical shape of the so-called stellar wind bubble described in Weaver et al. (1977), which is distorted into a stellar wind bow shock (Gull & Sofia 1979; Wilkin 1996) in the case of the 30% of runaway massive stars which move supersonically through the ISM (Blaauw 1961; Gies 1987; Gvaramadze et al. 2012; Moffat et al. 1998). Such bow shock can be observed throughout the whole electromagnetic spectrum, from the ultraviolet (Kaper et al. 1997) and the infrared waveband (Peri et al. 2012, 2015; Kobulnicky et al. 2016, 2017) to the high-energies (Benaglia et al. 2010; del Valle et al. 2013; De Becker et al. 2017). When the star evolves to the red supergiant phase, the wind interacts either with the interior of the main-sequence wind bubble (Garcia-Segura et al. 1996b,a; Freyer et al. 2006), or directly with the ISM if the star moves fast enough (Brighenti & D’Ercole 1995b; Chita et al. 2008; Herbst et al. 2022). The circumstellar medium of Wolf-Rayet stars takes the form

★ E-mail: dmameyer.astro@gmail.com

of circular rings in the context of fast-moving, high-latitude objects, bipolar nebulae in the case of rotating massive stars or more complex morphologies (Brighenti & D’Ercole 1995a; Meyer et al. 2020b; Meyer 2021). The surroundings of evolved massive stars is therefore the fingerprint of its past life onto the ISM, and, it constitutes the location of the supernova explosion. The supernova remnants left behind the death of high-mass stars are shaped by the interaction of the supernova shock wave with the circumstellar medium (Weiler & Sramek 1988). Unfolding them permit to reconstruct the past evolution and to constrain the properties of its progenitor star.

Supernova remnants of massive progenitor stars, or core-collapse supernova remnants, are characterised by the presence of circumstellar material enriched in the heavy elements synthesised by the progenitor released as stellar winds. They reveal the presence of elements such as Fe (Uchida et al. 2009), that have been produced in the core of the progenitor and by the possible presence of a neutron star left inside of the supernova remnant (Zavlin et al. 1998; Gvarnadamadze 2006), ultimately leading to the formation of pulsar wind nebulae (Olmi & Bucciantini 2023, 2019). The supernova explosion is closely connected to non-thermal physical mechanisms such as the anisotropic liberation of neutrinos (Kifonidis et al. 2006; Müller et al. 2012; Müller & Janka 2015) and the production of gravitational waves (Jardine et al. 2022). Models from the early instants (Aloy & Obergaulinger 2021) up to the first year of core-collapse event has been subject to numerical modelling in Gabler et al. (2021). The interaction of the liberated supernova shock wave with the last wind of the progenitor generates characteristic lightcurve functions of the wind properties, which have been observed and modelled (Chevalier 1982; Chevalier & Liang 1989; Truelove & McKee 1999). The propagating shock wave interacts with the circumstellar material before further expanding into the interstellar medium (Tutone et al. 2020), leading to the production of non-thermal emission (Orlando et al. 2019; Das et al. 2022). A well-documented example of such mechanism is that of Cassiopeia A (Finn et al. 2016; Holland-Ashford et al. 2020).

Once the shock wave further expands, its propagation is constrained by the distribution of circumstellar material shaped by the supernova progenitor, see e.g. the case of the historical core-collapse supernova remnant Kes 73 (Katsuda et al. 2018). The reflection towards the center of the explosion of the shock wave against its own circumstellar matter produces a central region emitting thermal X-rays that is surrounded by a radio shell. This class of supernova remnants is called mixed-morphology supernova remnant (Yusef-Zadeh et al. 2003; Arias et al. 2019; Chiotellis et al. 2019; Derlopa et al. 2019). Most evolved supernova remnants exhibit morphologies deviating from sphericity. These asymmetries might have many origins, such as the intrinsic asymmetry of the explosion (Orlando et al. 2020), but also the aspherical distribution of circumstellar material like an asymmetric (Blondin et al. 1996) wind or a bow shocks generated by runaway massive stars. The organised magnetic field of the ISM imposes stellar wind bubbles of massive stars an elongated morphology (van Marle et al. 2015), which, in its turn, imposes rectangular shapes to the supernova remnants (Meyer et al. 2022). On the long term, they can reflect in the subsequent pulsar wind nebulae of plerionic core-collapse supernova remnants (Meyer & Meliani 2022; Bandiera et al. 2023).

In this study, we explore by means of 2.5D MHD simulations the morphology and emission properties of core-collapse supernova remnants generated by runaway massive stars, including the rotation and magnetisation of the stellar winds. Furthermore, our approach made of high-resolution simulations using a uniform cylindrical grid (Meyer et al. 2015, 2020a, 2021b) is updated with the

inclusion of a system of passive scalar tracers which permit us to time-dependently follow the materials successfully expelled from the stellar surface throughout the many evolutionary phases undergone by the high-mass star. The circumstellar medium of the supernova progenitor is first simulated from the zero-age main-sequence of the star until the supernova time using methods similar to that of Comerón & Kaper (1998); van Marle et al. (2005, 2007, 2011); Mackey et al. (2012); van Marle et al. (2014); Meyer et al. (2014, 2016, 2017, 2020b); Green et al. (2019). Then, the early supernova-wind interaction is calculated in a one-dimensional fashion (Chevalier 1982; Truelove & McKee 1999; Dwarkadas 2005, 2007; Whalen et al. 2008; van Marle et al. 2010; Telezhinsky et al. 2012a,b, 2013; Chiotellis et al. 2013; Broersen et al. 2014) and mapped onto the circumstellar medium in order to model the evolution of the supernova remnant up to a time ~ 100 kyr after the explosion, see also Tenorio-Tagle et al. (1990, 1991); Velázquez et al. (2006); van Veelen et al. (2009); Vigh et al. (2011); Chiotellis et al. (2012); Toledo-Roy et al. (2014); van Marle et al. (2015); Fang et al. (2017); Chiotellis et al. (2020, 2021). By performing a resolution study, we discuss the internal organisation of the supernova remnants, such as the mixing of material at work therein, and, by radiative transfer calculation, we predict their non-thermal appearance by synchrotron emission.

This paper is organised as follows. First, the numerical methods used to model magnetised core-collapse supernova remnants of runaway, rotating, magnetised Wolf-Rayet-evolving massive stars are presented in Section 2. We detail the internal properties of the supernova remnants of a runaway $35 M_{\odot}$ progenitor in Section 3. We further discuss our results in Section 4 and finally draw our conclusions in Section 5.

2 METHOD

In this section we present the methods used to simulate the core-collapse supernova remnants of a runaway rotating magnetised $35 M_{\odot}$ massive star.

2.1 Governing equations

Our modelling of core-collapse supernova remnants is conducted within the frame of non-ideal magneto-hydrodynamics (Meyer et al. 2020b). The time evolution of a plasma volume element of the system is described by the mass continuity equation,

$$\frac{\partial \rho}{\partial t} + \nabla \cdot (\rho \mathbf{v}) = 0, \quad (1)$$

the equation for the conservation of linear momentum,

$$\frac{\partial \mathbf{m}}{\partial t} + \nabla \cdot (\mathbf{m} \otimes \mathbf{v} - \mathbf{B} \otimes \mathbf{B} + \hat{\mathbf{I}} p_t) = \mathbf{0}, \quad (2)$$

the total energy conservation equation,

$$\frac{\partial E}{\partial t} + \nabla \cdot ((E + p_t) \mathbf{v} - \mathbf{B}(\mathbf{v} \cdot \mathbf{B})) = \Phi(T, \rho), \quad (3)$$

and the equation for the evolution of the magnetic field,

$$\frac{\partial \mathbf{B}}{\partial t} + \nabla \cdot (\mathbf{v} \otimes \mathbf{B} - \mathbf{B} \otimes \mathbf{v}) = \mathbf{0}, \quad (4)$$

where $\mathbf{m} = \rho \mathbf{v}$ is the vector momentum, ρ the gas density, \mathbf{v} the flow velocity, p_t the total pressure and \mathbf{B} the magnetic field vector, respectively. The total energy of the system reads,

$$E = \frac{p}{(\gamma - 1)} + \frac{\mathbf{m} \cdot \mathbf{m}}{2\rho} + \frac{\mathbf{B} \cdot \mathbf{B}}{2}, \quad (5)$$

and the sound speed closing the system of equations Eq. 1-4 is defined as

$$c_s = \sqrt{\frac{\gamma p}{\rho}}, \quad (6)$$

with $\gamma = 5/3$ the adiabatic index.

Optically-thin radiative cooling and heating is included into the equations using the laws presented in Meyer et al. (2014). They are represented by the function,

$$\Phi(T, \rho) = n_H \Gamma(T) - n_H^2 \Lambda(T), \quad (7)$$

where

$$n_H = \frac{\rho}{\mu(1 + \chi_{\text{He},Z})m_H}, \quad (8)$$

is the hydrogen number density, with μ the adiabatic index, $\chi_{\text{He},Z}$ the solar helium and metal abundance, and where the quantity

$$T = \mu \frac{m_H}{k_B} \frac{p}{\rho}, \quad (9)$$

is the temperature of the gas, respectively. The functions Γ and Λ in Eq. 7 stand for the heating and cooling rates for photoionised gas per unit time. They account for cooling from H, He and metals Z (Wiersma et al. 2009) within the solar abundance (Asplund et al. 2009), which largely dominates the cooling at high T. It additionally includes components for hydrogen recombination (Hummer 1994), collisionally excited forbidden line emission for the metals of atomic number > 2 such as O, C and N (Raga et al. 1997). The heating rate represents the photon emitted by the photosphere of the massive star, which ionize the recombining hydrogenic ions and provoke the release of energetic electrons (Osterbrock & Bochkarev 1989).

The equations are integrated using the PLUTO code¹ (Mignone et al. 2007, 2012; Vaidya et al. 2018) using a Godunov-type solver composed of the shock-capturing HLL Rieman solver (Harten et al. 1983) and the eight-wave finite-volume algorithm (Powell 1997) for magnetised flows, which makes sure that the magnetic field remains divergence-free,

$$\vec{\nabla} \cdot \vec{B} = 0, \quad (10)$$

throughout the whole computational domain and over the entire simulation time, from the onset of the stellar wind to the middle-age evolution phase of the supernova remnant. It has been utilised in the precedent studies of the same authors devoted to the circumstellar medium of evolving and dying massive stars (Meyer et al. 2021c). Furthermore, the numerical scheme uses a third-order Runge-Kutta time integrator, the minmod flux limiter and the WENO3 interpolation scheme for the reconstruction of the primitive variables of the system. The time-marching algorithm is controlled by the Courant-Friedrich-Levy rule that is initialised to $C_{\text{eff}} = 0.1$ (Meyer 2021).

2.2 Modelling the circumstellar medium

2.2.1 Stellar wind density

The circumstellar medium of massive stars is modelled using a 2.5D cylindrical coordinate system (R,z) and a $[0; 100] \times [-50; 50]$ pc² computational domain of 8000×8000 grid zones. The stellar wind of the massive star is injected at the surface of a sphere of radius

$r_{\text{in}} 20$ cells centered onto the origin $O(0; 0; 0)$. The density is taken to be the profile

$$\rho_w(r = r_{\text{in}}, t) = \frac{\dot{M}(t)}{4\pi r^2 v_w(t)}, \quad (11)$$

where \dot{M} is the mass-loss rate of the massive star, v_w the terminal wind velocity of the star and r the radial direction. As in the previous papers of this series, the stellar wind nebula developing around the star is calculated in its reference frame. The stellar motion is mimicked by imposing a gas flow $v = -v_\star$ at the outer boundary of the computational domain at $z = 50$ pc, with $v_\star = 20$ pc the stellar speed through the ISM, see also Comerón & Kaper (1998); Green et al. (2019); Meyer et al. (2020b). The uniform ambient medium is in the warm phase of the ISM, with a temperature of $T_{\text{ISM}} \approx 8000$ K and a magnetisation of $B_{\text{ISM}} = 7 \mu\text{G}$ taken to be parallel to the Oz symmetry axis of the computational domain (Meyer et al. 2017).

2.2.2 Stellar wind velocity

The stellar wind properties of the massive star that we consider are shown in Fig. 1. The figure plots the time evolution of various stellar global and surface quantities such as the stellar mass M_\star (Fig. 1a), the stellar radius R_\star (Fig. 1b), the effective temperature T_{eff} (Fig. 1c), as well as the mass-loss rate (Fig. 1d), that are directly taken from the stellar evolution model of the GENEVA library² (Ekström et al. 2012) with an initial mass of $35 M_\odot$ and a rotation velocity of

$$\frac{\Omega_\star(t=0)}{\Omega_K} = 0.1, \quad (12)$$

and with

$$\Omega_\star(t) = \frac{v_{\text{rot}}(t)}{R_\star(t)} \quad (13)$$

the angular frequency of the star and Ω_K the equatorial Keplerian velocity. The star undergoes three distinct evolutionary phase, i.e. a hot main-sequence with a mass-loss rate of $\dot{M} \approx 10^{-6.3} M_\odot \text{yr}^{-1}$ lasting at time ≈ 5.1 Myr, a short, ≈ 0.25 Myr-long cold red supergiant phase with a dense wind of $\dot{M} \approx 10^{-4.0} M_\odot \text{yr}^{-1}$ and a final Wolf-Rayet phase with $\dot{M} \approx 10^{-5.0} M_\odot \text{yr}^{-1}$. The star loses most of its mass during the two last phases (Fig. 1a) and the supernova time is at ≈ 0.63 Myr. The wind terminal velocity is calculated as

$$\frac{v_w(t)}{v_{\text{esc}}(t)} = \sqrt{\beta(T)}, \quad (14)$$

or equivalently,

$$v_w(t) = \sqrt{\beta(T) \frac{2GM_\star(t)}{R_\star(t)}}, \quad (15)$$

with the escape speed of the massive star $v_{\text{esc}}(t)$, its stellar radius $R_\star(t)$ (Fig. 1b), and

$$\beta_w(T) = \begin{cases} 1.0 & \text{if } T_{\text{eff}} \leq 10000 \text{ K}, \\ 1.4 & \text{if } T_{\text{eff}} \leq 21000 \text{ K}, \\ 2.65 & \text{if } T_{\text{eff}} > 21000 \text{ K}, \end{cases} \quad (16)$$

a corrective factor that is function of the effective temperature (El-Idrissi et al. 2006), see Fig. 1c. The evolution of v_w decreases as a function of time, as the main-sequence wind is supersonic ($\approx 1800 \text{ km s}^{-1}$), the red supergiant wind velocity is very slow ($\approx 30 \text{ km s}^{-1}$) and the final Wolf-Rayet wind velocity increases up to ($\approx 700 \text{ km s}^{-1}$), see Fig. 1e.

¹ <http://plutocode.ph.unito.it/>

² <https://www.unige.ch/sciences/astro/evolution/en/database/syclist/>

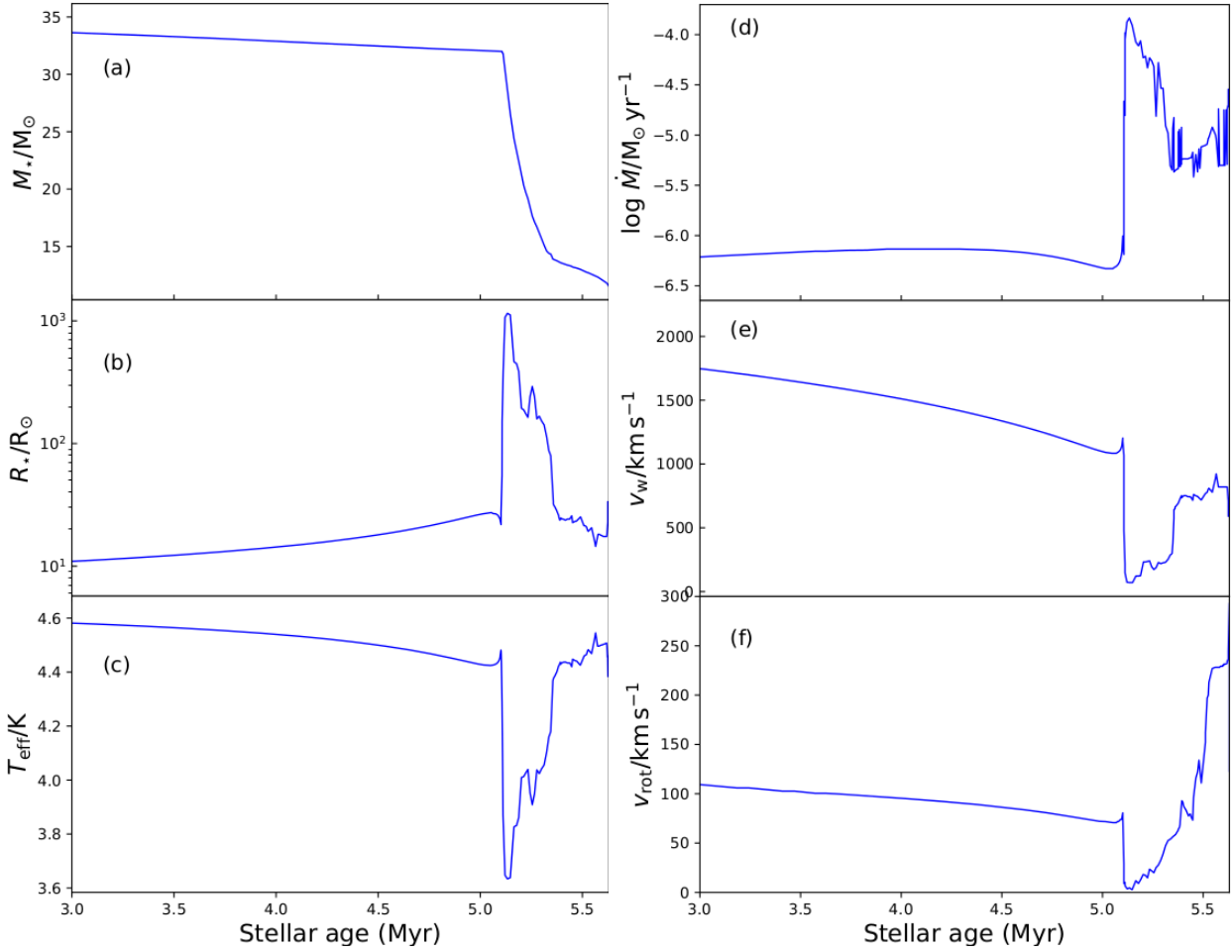


Figure 1. Surface and stellar wind properties of a $35 M_{\odot}$ supernova progenitor. The left-hand figures display the time evolution of the stellar mass M_{\star} (in M_{\odot} , panel a), the stellar radius R_{\star} (in R_{\odot} , panel b), the effective temperature T_{eff} (in K, panel c). The right-hand figures show the mass-loss rate \dot{M} (in $M_{\odot} \text{ yr}^{-1}$, panel d), the terminal wind velocity v_w (in km s^{-1} , panel e) and the equatorial rotation profile of the star v_{rot} (in km s^{-1} , panel f), respectively.

2.2.3 Stellar rotation and magnetic field

The stellar magnetic field is imposed at the inner stellar wind boundary as a Parker spiral (Parker 1958; Weber & Davis 1967; Pogorelov & Semenov 1997; Pogorelov & Matsuda 2000) that is superimposed to the stellar wind (Chevalier & Luo 1994; Rozyczka & Franco 1996; García-Segura et al. 2018, 2020). It is composed of both a radial

$$B_r(r, t) = B_{\star}(t) \left(\frac{R_{\star}(t)}{r} \right)^2, \quad (17)$$

and of a toroidal component

$$B_{\phi}(r, t) = B_r(r, t) \left(\frac{v_{\phi}(\theta, t)}{v_w(t)} \right) \left(\frac{r}{R_{\star}(t)} - 1 \right), \quad (18)$$

respectively, with

$$v_{\phi}(\theta, t) = v_{\text{rot}}(t) \sin(\theta), \quad (19)$$

the latitude-corrected azimuthal component of the surface stellar velocity, where the factor $\sin(\theta)$ account for the latitude-dependence of the surface rotation (Fig. 1f). The third poloidal component of the magnetic field is set to $B_{\theta} = 0$ G. As the magnetic field is transported into the stellar wind of the massive star, we scale the decrease of the strength of the surface magnetic field to that of the Sun, via the relation

$$\frac{B_{\star}(t)}{B_{\odot}} = \frac{B_w(t, r = 1 \text{ au})}{B_{w, \odot}(r = 1 \text{ au})}, \quad (20)$$

where $B_w(t, r = 1 \text{ au})$ is the star's magnetic field at a distance of $r = 1 \text{ au}$ from the stellar center, B_{\odot} the Sun's surface magnetic field and $B_{w, \odot}(r = 1 \text{ au})$ the observed strength of the magnetic field in the solar wind, respectively. This recipe has been used as an addition to boundary conditions for magnetised stellar winds in the context of massive stars (Scherer et al. 2020; Herbst et al. 2020; Baalman et al. 2020, 2021; Meyer et al. 2021c).

The time-dependence of the stellar surface magnetic field $B_{\star}(t)$ is estimated by assuming a typical field strength for each individual evolutionary phase of the massive star. The main-sequence field is taken to $B_{\star} = 500 \text{ G}$ (Fossati et al. 2015; Castro et al. 2015; Przybilla et al. 2016; Castro et al. 2017). Regarding the red supergiant phase, we use the value derived for Betelgeuse, i.e. $B_{\star} = 0.2 \text{ G}$ (Vlemmings et al. 2002, 2005; Kervella et al. 2018). Finally, we assume the ad-hoc value of $B_{\star} = 100 \text{ G}$ for the final Wolf-Rayet phase (Meyer 2021). These assumed values are reported in Fig. 2a and permit to build a magnetic field history at any radius of the stellar wind boundary $r = r_{\text{in}}$, see Fig. 2b.

2.2.4 Mixing of materials

Last, a system of passive scalar tracers permit us to time-dependently follow the evolution and mixing of stellar wind materials into the circumstellar medium and the supernova remnant. Since the $35 M_{\odot}$

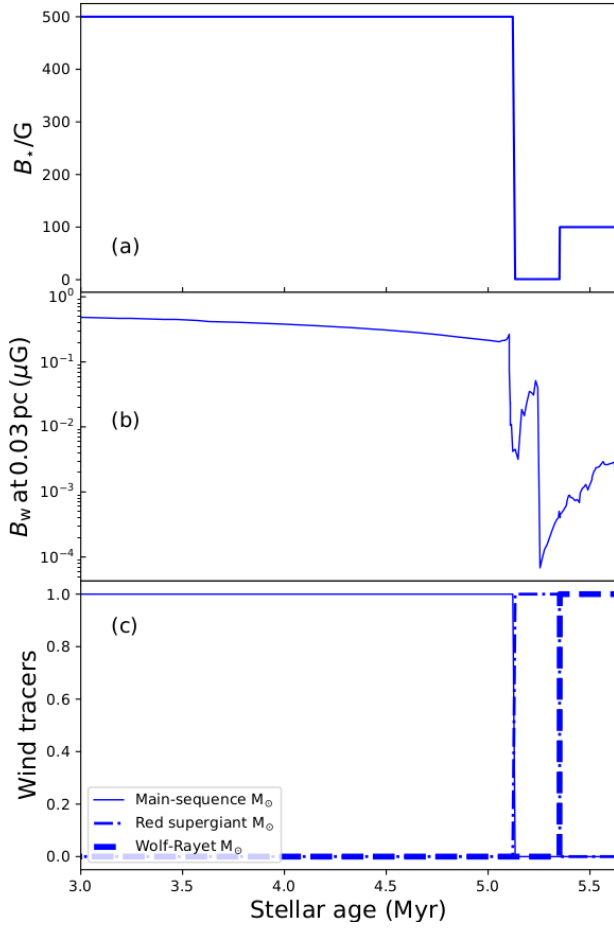


Figure 2. Temporal evolution of the surface magnetic field strength, B_* , (panel a), the magnetic field strength in the stellar wind, B_w , at $r = 0.03$ au from the star (panel b), and the values of the passive scalar tracers (panel c) for the different wind phases of the stellar evolution.

of the GENEVA library (Ekström et al. 2012) undergoes three typical evolutionary phases, i.e. an initial long main-sequence phase, a supergiant phase and final Wolf-Rayet phase, we introduce the corresponding tracers Q_{MS} , Q_{RSG} and Q_{WR} , obeying the continuity equations

$$\frac{\partial(\rho Q_{MS})}{\partial t} + \nabla \cdot (v \rho Q_{MS}) = 0, \quad (21)$$

$$\frac{\partial(\rho Q_{RSG})}{\partial t} + \nabla \cdot (v \rho Q_{RSG}) = 0, \quad (22)$$

and

$$\frac{\partial(\rho Q_{WR})}{\partial t} + \nabla \cdot (v \rho Q_{WR}) = 0, \quad (23)$$

respectively. The initial value of the passive scalar is set to $Q_i = 1$ during the time the star spends in the evolutionary phase $i = \{MS, RSG, WR\}$ and $Q_i = 0$ otherwise. This implies that $Q_{MS} + Q_{RSG} + Q_{WR} = 1$ at every time of the simulation at the stellar wind boundary $r = r_{in}$.

2.3 Modelling the ejecta-wind interaction

The interaction between the supernova ejecta and the isotropic freely-expanding stellar wind of the progenitor is calculated using a 1D

spherically-symmetric computational domain $[O; r_{out}]$. The supernova ejecta initially occupy the $0 \leq r \leq r_{max} < r_{out}$ region of the domain. The corresponding density field reads,

$$\rho(r) = \begin{cases} \rho_{core}(r) & \text{if } r \leq r_{core}, \\ \rho_{max}(r) & \text{if } r_{core} < r < r_{max}, \end{cases} \quad (24)$$

where $0 < r_{core}$ is filled by the constant high-density plateau

$$\rho_{core}(r) = \frac{1}{4\pi n} \frac{(10E_{ej}^{n-5})^{-3/2}}{(3M_{ej}^{n-3})^{-5/2}} \frac{1}{t_{max}^3}, \quad (25)$$

while the ejecta velocity display an homologous expansion

$$v(r) = \frac{r}{t}, \quad (26)$$

which is reaching

$$v_{core} = \left(\frac{10(n-5)E_{ej}}{3(n-3)M_{ej}} \right)^{1/2} \quad (27)$$

at a distance $r = r_{core}$ from the center of the explosion, respectively. The region $r_{core} \leq r \leq r_{max}$ contains the envelope of ejecta made of material of decreasing density,

$$\rho_{max}(r) = \frac{1}{4\pi n} \frac{(10E_{ej}^{n-5})^{(n-3)/2}}{(3M_{ej}^{n-3})^{(n-5)/2}} \frac{1}{t_{max}^3} \left(\frac{r}{t_{max}} \right)^{-n}, \quad (28)$$

with $n = 11$, see Chevalier (1982); Truelove & McKee (1999). At the edge of the supernova shock wave the gas flow speed is $v_{max} = 30000 \text{ km s}^{-1}$, defining the time at which we start the simulations,

$$t_{max} = \frac{r_{max}}{v_{max}}, \quad (29)$$

and r_{max} is found using the numerical procedure of van Veelen et al. (2009).

In the above relations, $E_{ej} = 5 \times 10^{50} \text{ erg}$ is the energy released by the supernova explosion, and,

$$M_{ej} = M_{\star} - \int_{t_{ZAMS}}^{t_{SN}} \dot{M}(t) dt - M_{NS} = 10.12 M_{\odot}, \quad (30)$$

is the ejecta mass, with t_{ZAMS} and t_{SN} the zero-age main-sequence and supernova times of the evolution of the $35 M_{\odot}$ that we consider, and $M_{NS} = 1.4 M_{\odot}$ the mass of the neutron star left behind the dead progenitor.

2.4 Modelling the supernova remnant

The 1D ejecta-wind interaction is mapped onto a 2.5D computational domain of size $[0; 45] \times [-45; 45] \text{ pc}^2$ before the supernova shock wave reaches the termination shock of the Wolf-Rayet stellar wind, which corresponds to a circle of radius 2.45 pc centered onto the origin. The mixing of the ejecta into the circumstellar medium at the pre-supernova time is traced by a passive scalar Q_{EJ} advected via,

$$\frac{\partial(\rho Q_{EJ})}{\partial t} + \nabla \cdot (v \rho Q_{EJ}) = 0, \quad (31)$$

and whose value is initially set to $Q_{EJ} = 1$ in the ejecta at time t_{max} and to $Q_{EJ} = 0$ in the rest of the circumstellar and interstellar medium, respectively.

In this study, we focus on the case of a $35 M_{\odot}$ star that is static or moving with velocity $v_{\star} = 20\text{--}40 \text{ km s}^{-1}$ in a uniform medium of number density 0.79 cm^{-3} , which implies that the supernova progenitor moves with a Mach number $M \approx 0, 1$ and 2 , respectively.

Table 1. List of models and spatial resolution adopted in each simulation.

Model	Grid mesh
Run-35-MHD-0-SNR	$3000 \times 6000^{(a)}$
Run-35-MHD-20-SNR-1000	1000×2000
Run-35-MHD-20-SNR-2000	2000×4000
Run-35-MHD-20-SNR-4000	4000×8000
Run-35-MHD-20-SNR-8000	8000×16000
Run-35-MHD-40-SNR-2000	2000×4000

(a) [Meyer et al. \(2022\)](#)

The supernova remnants are calculated with a grid resolution of 2000×4000 grid zones, while we perform a resolution study with the model with $v_\star = 20 \text{ km s}^{-1}$. For reference, we compare our results with the supernova remnant model with $v_\star = 0 \text{ km s}^{-1}$ of [Meyer et al. \(2022\)](#). We list the ensemble of performed models in Table 1.

3 RESULTS

This section presents the modelled core-collapse supernova remnant generated by a Wolf-Rayet-evolving runaway massive progenitor star moving at velocity $v_\star = 20 \text{ km s}^{-1}$ and $v_\star = 40 \text{ km s}^{-1}$. We begin to present the pre-supernova circumstellar medium and the evolution of the supernova remnants. We focus on the internal properties of the supernova remnants, their luminosities and the mixing of material happening therein.

3.1 The pre-supernova circumstellar medium

Fig. 3 displays circumstellar medium at the supernova time in our MHD simulations of massive runaway stars moving with velocity $v_\star = 20 \text{ km s}^{-1}$ (panel a) and $v_\star = 40 \text{ km s}^{-1}$ (panel b). The figures represent the number density field (in cm^{-3}) in the models and their right-hand part plots the ISM magnetic field lines (black arrows) vertical to the symmetry axis and penetrating the region of shocked material. The density field is structured as a large-scale bow shock generated during the main-sequence phase of the star's life. It has the standard features of the astrophysics of moving stellar objects, with a bow shock facing the direction of stellar motion, separated from the star by a stand-off distance ([Baranov et al. 1971](#)),

$$R_{\text{SO}} = \sqrt{\frac{\dot{M} v_\star}{4\pi \rho_{\text{ISM}} v_\star^2}}, \quad (32)$$

with ρ_{ISM} the mass density of the ISM material, and which overall shape can be approximated by,

$$R(\theta) = R_{\text{SO}} \frac{\sqrt{3(1-\theta)\cotan(\theta)}}{\sin(\theta)}, \quad (33)$$

where θ is the angle from the direction of stellar motion ([Wilkin 1996](#)). A tubular low-density region shaped by the winds and a central circular cavity surrounded by a Wolf-Rayet shell are found at the apex of the bow shock. A series of contours trace the regions made of 50% in number density of each kind of material, such as the main-sequence stellar wind (blue), the red supergiant (red) and the Wolf-Rayet (purple) stellar winds as well as the supernova ejecta (green).

The cone of the bow shock behind the star is more opened in the case of the star moving with $v_\star = 20 \text{ km s}^{-1}$ (Fig. 3a) than in the case of the faster-moving star (Fig. 3b). The Wolf-Rayet wind, faster than

the speed of stellar motion v_\star , forms a shell of evolved stellar wind and swept-up ISM gas when interacting bow shock ([Brighenti & D'Ercole 1995a,b](#)). The circumstellar medium of the faster-moving star is affected by Rayleigh-Taylor instabilities, both ahead of the bow shock where large eddies are seen, and in the tubular cavity in the wake of the star, which close it and separate the main-sequence material from the other winds (Fig. 3b). The environment of the slower-moving stellar object displays a region of red supergiant material (red) separating the main-sequence wind (blue) from the Wolf-Rayet material (purple). Hence, the mixing of post-main-sequence materials is also at work before the supernova explosion when the star moves slowly, because of the size and unstable character of the low-density channel (Fig. 3a). Conversely, the supernova ejecta of the fast-moving star are released in a closed bubble of radius $\approx 10 \text{ pc}$ centered onto the location of the defunct star (Fig. 3a), whereas the direct environment of the supernova of the slowly moving star is open to the trail of the bow shock (Fig. 3a).

3.2 Supernova remnants

The next panels of Fig. 3 show the evolution of the supernova remnants at times 8 kyr (middle line) and at time 80 kyr for the model with $v_\star = 20 \text{ km s}^{-1}$ (left) and $v_\star = 40 \text{ km s}^{-1}$ (right). They plot the reverberation of the supernova shock wave against the walls of the asymmetric Wolf-Rayet cavity at work in the remnants, together with the subsequent game of reflections and transmissions of waves happening in it. The imprint of the morphology of that Wolf-Rayet cavity already strongly modifies the geometry of the expanding forward shock at time 8 kyr. The ejecta filled the region between the center of the explosion and the former termination shock of the pre-supernova bow shock, and the reverberated shock towards the center of the explosion carries the imprint of the distribution of Wolf-Rayet wind, see black contour for the region of gas hotter than 10^6 K in Fig. 3c and Fig. 3d. The red supergiant material (red) is distributed as a thin layer surrounding the ejecta region (green), and it has started to efficiently mix with the Wolf-Rayet material (purple) in the direction opposite of that of the progenitor's motion. Note that the red supergiant material distributes, because of the morphology of the instabilities of the pre-supernova circumstellar medium, as knots in the case of our faster-moving progenitor (Fig. 3d).

The bottom series of panels in Fig. 3 display the supernova remnants at a later time of their evolution. The reverberated supernova shock wave propagated all through the cavity and experienced a second reflection against the walls of the cavity. The overall remnant has grown in size and a top region of shocked ejecta and ISM gas expanding into the unperturbed ISM is clearly visible. It is more pronounced in the model with $v_\star = 40 \text{ km s}^{-1}$ as a result of the smaller amount of mass in the Wolf-Rayet shell ([Meyer et al. 2015](#)). The old supernova remnant is shaped as a Cygnus-loop-like nebulae in the model with $v_\star = 20 \text{ km s}^{-1}$ as a result of the channelling of the supernova shock wave into the tunnel of low-density cavity, while that generated by the progenitor moving with $v_\star = 40 \text{ km s}^{-1}$ harbors a more ovoid morphology. The external envelope of the supernova remnant does not develop large scale instabilities as a result of the background ISM magnetic field ([Meyer et al. 2021b](#)). The Wolf-Rayet material is entirely mixed with the other kind of material, except in some very small punctual regions (Fig. 3f), and the red supergiant material has efficiently mixed with the supernova ejecta. The main-sequence material is advected downstream the remnant and does not contribute to its composition.

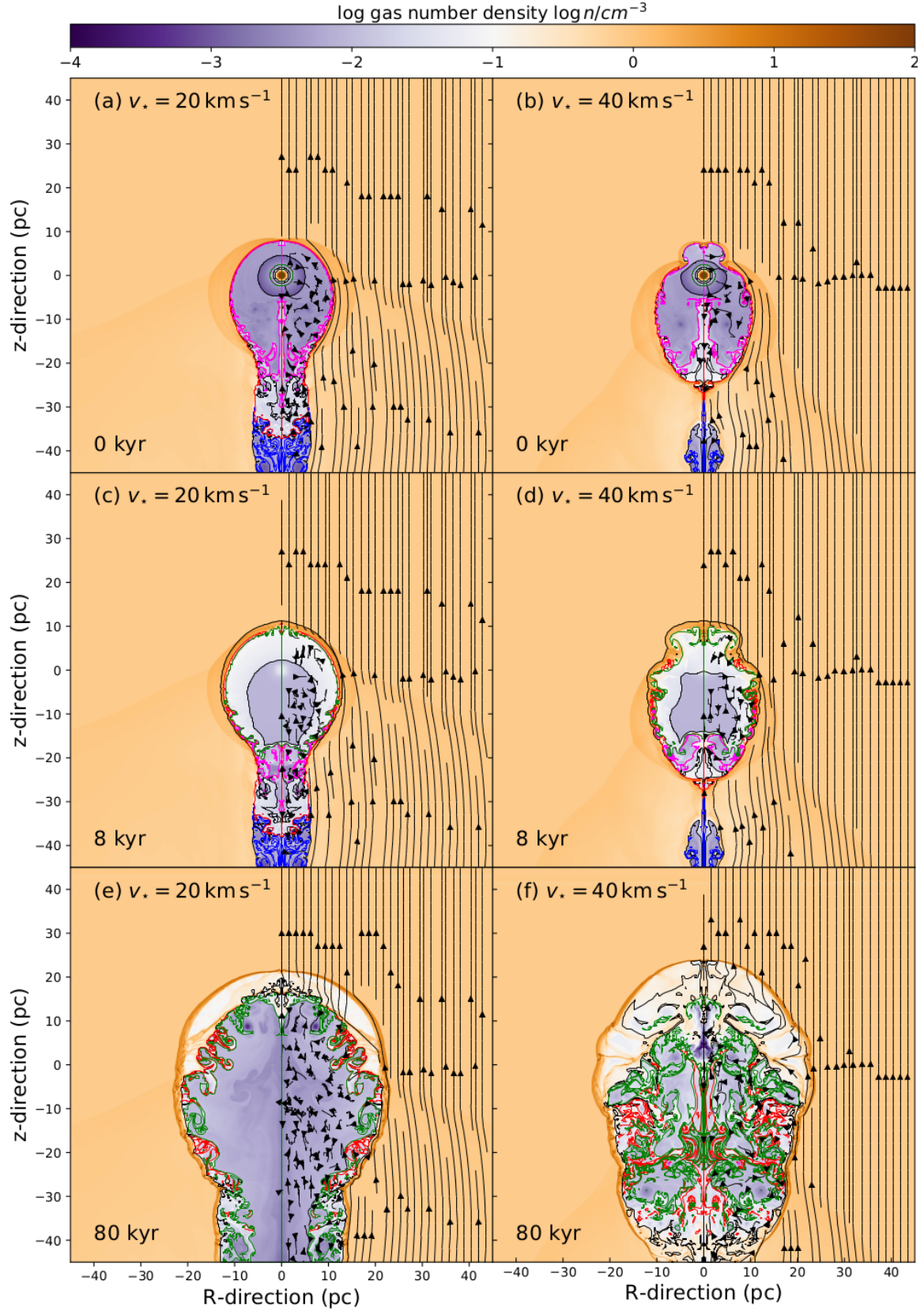


Figure 3. Number density fields in our magneto-hydrodynamical simulation of the supernova remnant of the runaway $35 M_{\odot}$ star rotating with $\Omega_*/\Omega_K = 0.1$ and moving with velocity $v_* = 20 \text{ km s}^{-1}$ (left) and $v_* = 40 \text{ km s}^{-1}$ (right). The various contours highlight the region with a 50% contribution of supernova ejecta (green), Wolf-Rayet wind (purple), red supergiant wind (red), main-sequence material (blue), respectively. The black lines are iso-temperature contours ($T = 10^6 \text{ K}$) and the black arrows are magnetic field lines.

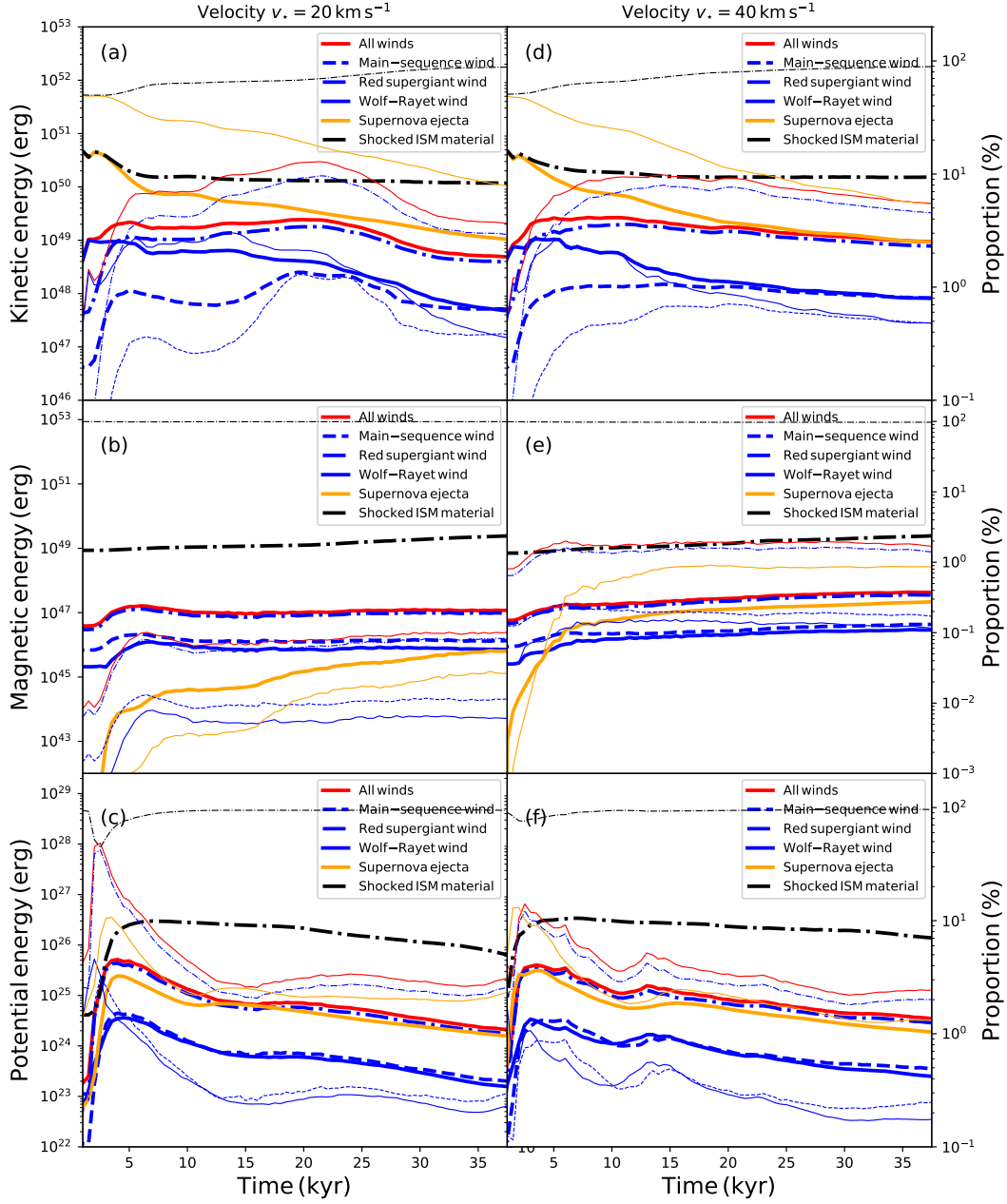


Figure 4. Energy evolution in the supernova remnant (thick lines) as a function of time, for different simulations with velocity $v_{\star} = 20$ (left) and 40 km s^{-1} (right). The figure displays the kinetic (top panel), magnetic (middle panel) and potential components (bottom panel) of the total energy. Each panel distinguishes between the contribution from the stellar wind (red solid line), main-sequence material (dashed blue line), red supergiant material (dashed dotted blue line), Wolf-Rayet gas (solid blue line), supernova ejecta (solid orange line) and shocked ISM gas (dashed dotted black line). The thin lines give the corresponding percentages of the total energy at a function of time.

3.3 Energetics

Fig. 4 displays the kinetic (top), magnetic (middle) and potential energy (bottom) energies in the supernova remnants of progenitors moving with velocity $v_{\star} = 20 \text{ km s}^{-1}$ (left) and $v_{\star} = 40 \text{ km s}^{-1}$ (right). Each figure distinguishes between the components from the main-sequence (dashed blue line), red supergiant (dotted dashed blue line), Wolf-Rayet (solid blue line) stellar winds, the supernova ejecta (orange), and the ISM material (dashed dotted black line). The kinetic

energy of a given species i is calculated as,

$$E_{\text{kin}}^i = \mu m_{\text{H}} \iint_{\text{SNR}} n |\vec{v}|^2 Q_i dV, \quad (34)$$

by integrating the kinetic energy density over the entire supernova remnant, with Q_i the tracer associated to the considered species and dV the volume element. Similarly, the magnetic energy of the gas is defined as,

$$E_{\text{mag}}^i = \iint_{\text{SNR}} \frac{|\vec{B}|^2}{2} Q_i dV, \quad (35)$$

and, finally, the potential energy in the supernova remnant reads,

$$E_{\text{int}}^i = \mu m_H \iint_{\text{SNR}} n \epsilon Q_i dV = \mu m_H \iint_{\text{SNR}} n \frac{p}{(\gamma - 1)} Q_i dV, \quad (36)$$

where $\epsilon = p/(\gamma - 1)$ is the internal energy density. These quantities are evaluated throughout the supernova remnant simulation, up to a time 40 kyr.

In both models, the kinetic component of the energy budget of the supernova remnant ($E_{\text{kin}} \sim 10^{50}$ erg) is more important than that of the magnetic ($E_{\text{mag}} \sim 10^{49}$ erg) and internal potential ($E_{\text{pot}} \sim 10^{26}$ erg) energy. The decreasing evolution of the ratio $E_{\text{kin}}/E_{\text{mag}}$ that in middle-age (30–35 kyr) core-collapse supernova remnants E_{mag} accounts for about 10% of the energy of the supernova remnant and should not be neglected into the simulations. The kinetic energy of the supernova remnant whose progenitor moves with velocity $v_\star = 20 \text{ km s}^{-1}$ is initially such that $E_{\text{kin}}^{\text{ISM}} \sim E_{\text{kin}}^{\text{ej}}$ and the stellar wind does not contribute much to the energy budget $E_{\text{kin}}^{\text{wind}} \ll E_{\text{kin}}^{\text{ej}} + E_{\text{kin}}^{\text{ISM}}$, see Fig. 4a. The wind contribution is governed by the red supergiant material. Then, the ejecta kinetic energy diminishes because of the deceleration of the blastwave which enters the Sedov-Taylor phase once it interacts with the circumstellar medium of the progenitor and sweeps up more of that material than the mass of the ejecta. The situation is similar in the model with progenitor's velocity $v_\star = 40 \text{ km s}^{-1}$, although we note an energetically more important main-sequence wind in the first 15 kyr of the remnant's life (Fig. 4d). This is due to the thinner, more unstable cavity of unshocked stellar wind left behind the progenitor in the case of a fast-moving star, which prevents the ejecta to interact directly with the main-sequence material, see Fig. 3.

The magnetic energy E_{mag} of the gas constituting the supernova remnant is about two orders of magnitude smaller than the kinetic energy E_{kin} . Within the many materials inside of the supernova remnant, the ejecta contributes less than one per cent to E_{mag} , because in our models the unshocked supernova material is initially unmagnetised (Section 2.3). The shocked ejecta compress the stellar wind and the circumstellar magnetic field lines, which mix with the ejecta as the blastwave does through the material of the wind-blown bubble. The contribution from the stellar wind is governed by the red supergiant material, while the main-sequence gas, and, to an even larger extent the Wolf-Rayet material are negligible to the magnetic energy ($E_{\text{mag}}^{\text{RSG}} > E_{\text{mag}}^{\text{MS}}$ and $E_{\text{mag}}^{\text{RSG}} > E_{\text{mag}}^{\text{WR}}$). The denser surroundings generated by the progenitor moving with velocity $v_\star = 40 \text{ km s}^{-1}$ induce a slightly more magnetised remnant (Fig. 4e). The internal contribution to the total energy of the supernova remnant is very small (Fig. 4c,f). It is regulated by the shocked ISM material (90%), the red supergiant material weights for 1% of the internal energy while the other winds (main-sequence and Wolf-Rayet) have negligible contributions to E_{int} .

3.4 X-rays luminosities

Fig. 5 displays the hard (top) and soft (bottom) X-ray lightcurves of the supernova remnants of the progenitors moving with velocity $v_\star = 20 \text{ km s}^{-1}$ (left) and $v_\star = 40 \text{ km s}^{-1}$ (right). As in Fig. 4, the different stellar winds, the supernova ejecta, and the ISM material are separated using the system of passive scalar tracers. For a given species, the X-ray luminosity at energy $E \geq \alpha \text{ keV}$ is estimated as,

$$L_{X_{E \geq \alpha}}^i = \iint_{\text{SNR}} j_X^{E \geq \alpha}(T) n_H^2 Q_i dV, \quad (37)$$

where j_X is the emissivity for diffuse ISM obtained with the `xSPEC` software (Arnaud 1996). Therefore, the luminosity in a specific en-

ergy band reads,

$$L_{X_{\alpha \leq E \leq \beta}}^i = \iint_{\text{SNR}} \left(j_X^{E \leq \beta}(T) - j_X^{\alpha \leq E}(T) \right) n_H^2 Q_i dV, \quad (38)$$

and we perform such integral for the $0.1 \leq E \leq 5.0 \text{ keV}$ (soft) and $E \geq 5.0 \text{ keV}$ (hard).

The overall hard X-ray luminosities, dominated by the ejecta and the shocked ISM, abruptly increase when the supernova shock wave hits the circumstellar material, before decreasing with time as the gas temperature lessens (thick lines of Figs. 5a,b). Further mild variations at time 15 kyr mirror the reverberation of the ejecta in the center of the remnants. The hard stellar-wind contribution in the model with $v_\star = 20 \text{ km s}^{-1}$ accounts for $< 10\%$ of the soft L_X , while the ISM and the ejecta represent $\approx 40\%$ each. In the model with $v_\star = 40 \text{ km s}^{-1}$, the wind contribution is more important, especially at the moment of the reflection of the shock wave inside of the remnant, when it can reach up to $\approx 40\%$ and exceed that of the ISM plus ejecta (thin lines of Figs. 5a,b). On the contrary, the total soft X-ray luminosity increases and reaches a plateau largely governed by the radiation from ISM material which exceeds the luminosity in hard X rays by several orders of magnitude. Note that the ejecta contribution to the soft X-ray luminosity is about 20% as its temperature is too hot ($T \geq 10^6 \text{ K}$) and that the stellar wind contribution is negligible once the shock wave has interacted with the circumstellar medium (at times 5 kyr).

Interestingly, the main-sequence wind contribution in the hard X-ray band is the smallest of all winds, while it is that of the Wolf-Rayet wind which is the least emitting in the soft X rays. In both wavebands, the red supergiant material dominates the stellar wind contributions to the total luminosity. This can be explained since the main-sequence wind is rapidly advected downstream in the ejecta-wind interaction region by the stellar motion. The Wolf-Rayet material efficiently mixes inside of the supernova remnant up to being confined in small regions scattering inside of it (Fig. 3).

3.5 Mixing of materials in the supernova remnant

Fig. 6 plots the volume evolution of the remnants whose progenitors are moving with velocity $v_\star = 20 \text{ km s}^{-1}$ (top) and $v_\star = 40 \text{ km s}^{-1}$ (bottom). Each figure distinguishes the components from the main-sequence (dashed blue line), red supergiant (dotted dashed blue line), Wolf-Rayet (solid blue line) stellar winds, the supernova ejecta (orange), and the ISM material (dashed dotted black line). Most of the supernova remnants are filled with shocked ISM material (see dashed dotted thick black lines in Fig. 6a,b) which occupies about 80–90% of its volume, all the other species representing about 10–20% of the remaining volume. The volume of the remnant is constant in our simulation because it is calculated taking into account pre-supernova circumstellar medium, which does not evolve much after the time of the explosion. However, the volume filled by the ejecta quickly increases after the explosion during the freely expanding phase of the blastwave ($\leq 5 \text{ kyr}$ after the explosion) and its proportion of occupied volume reaches $\approx 15\%$ in the model with $v_\star = 20 \text{ km s}^{-1}$ (Fig. 6a) and $\approx 10\%$ $v_\star = 40 \text{ km s}^{-1}$ (Fig. 6b) since the cavity of the slowly-moving progenitor is larger than that of the fast-moving one (Fig. 3). The other stellar wind materials, which very initially fill more space than the ejecta, quickly shrink as the blastwave propagates and mixes with the Wolf-Rayet stellar wind. At time $\leq 10 \text{ kyr}$ this induces a transition between the wind material in the remnant being mostly made of Wolf-Rayet gas to a stage in which the red supergiant gas dominates.

Fig. 7 displays the mixing factor for the different kind of materials

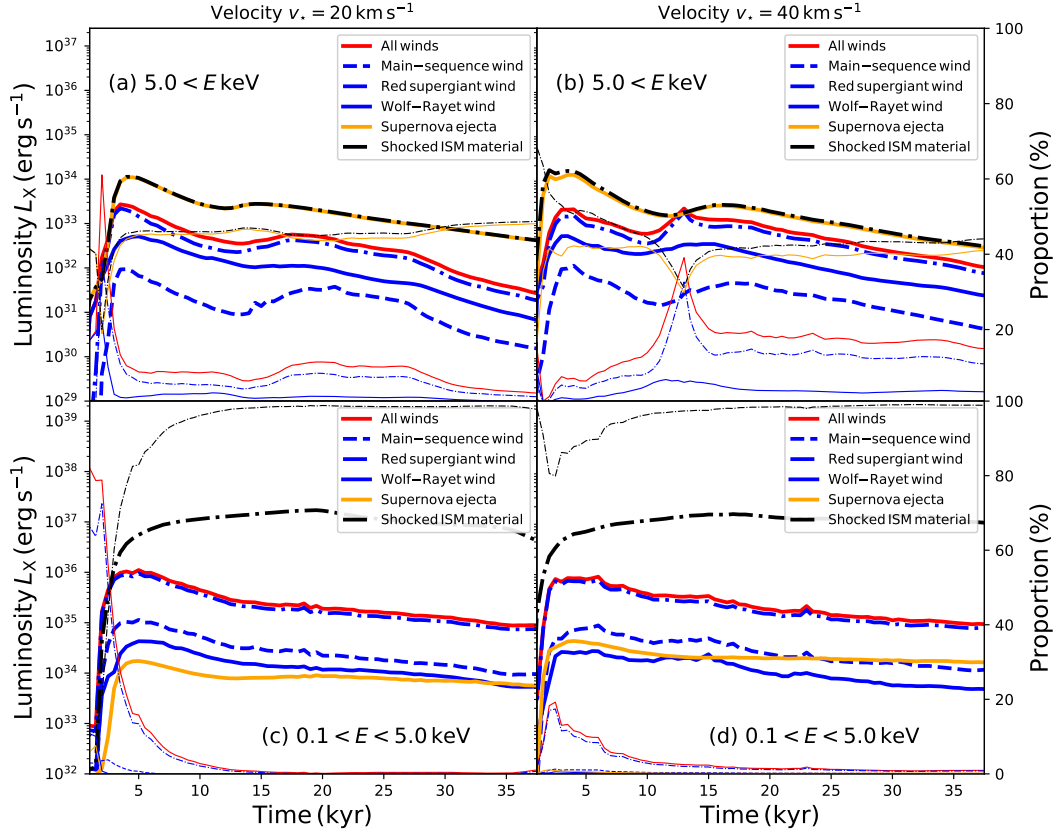


Figure 5. Soft X-ray (bottom) and hard X-ray (top) lightcurves of the supernova remnant. Each panel distinguishes the contribution from the stellar wind (red solid line), main-sequence material (dashed blue line), red supergiant material (dashed dotted line), Wolf-Rayet gas (solid blue line), supernova ejecta (solid orange line) and shocked ISM gas (dashed dotted black line). We also show the time evolution of the relative contributions to the energy budget for each species in the simulation (thin lines, in per cent).

present in the supernova remnants of the progenitors moving with $v_{\star} = 20 \text{ km s}^{-1}$ (dashed red line) and with $v_{\star} = 40 \text{ km s}^{-1}$ (dotted dashed blue line). We define the mixing factor of the main sequence,

$$f_{\text{MS}} = \frac{\mu m_{\text{H}} \iint_{Q_{\text{MS}} \leq 0.5} n Q_{\text{MS}} dV}{\mu m_{\text{H}} \iint_{\text{SNR}} n Q_{\text{MS}} dV} = \frac{\iint_{Q_{\text{MS}} \leq 0.5} n Q_{\text{MS}} dV}{\iint_{\text{SNR}} n Q_{\text{MS}} dV}, \quad (39)$$

the red supergiant,

$$f_{\text{RSG}} = \frac{\iint_{Q_{\text{RSG}} \leq 0.5} n Q_{\text{RSG}} dV}{\iint_{\text{SNR}} n Q_{\text{RSG}} dV}, \quad (40)$$

and the Wolf-Rayet

$$f_{\text{WR}} = \frac{\iint_{Q_{\text{WR}} \leq 0.5} n Q_{\text{WR}} dV}{\iint_{\text{SNR}} n Q_{\text{WR}} dV}, \quad (41)$$

stellar winds, respectively. The mixing factor of the ejecta is similarly defined,

$$f_{\text{ej}} = \frac{\iint_{Q_{\text{ej}} \leq 0.5} n Q_{\text{ej}} dV}{\iint_{\text{SNR}} n Q_{\text{ej}} dV}, \quad (42)$$

where the numerator is the mass with subdominant ejecta fraction and where the denominator is the initial mass of that same material, see [Orlando et al. \(2005\)](#). For $f = 0$ no mixing at all has taken place inside of the remnant while for $f = 1$ most ejecta material is

dispersed into volume elements to which it contributes $< 50\%$ in number density.

At the beginning of the simulation, the main-sequence material is already fairly mixed to a fraction $\geq 95\%$, regardless of the motion of the progenitor star (Fig. 7a). We consider only the circumstellar medium at distance $< 50 \text{ pc}$ from the location of the explosion and use it to initialise the simulations, which ignores the long trail of main-sequence material behind the star (Fig. 3). Hence, the main-sequence material in the computational domain only represents that expelled by the star before the onset of the red supergiant phase. The mixing factor increases 15 – 20 kyr after the explosion, when the ejecta, channelled into the low-density cavity, pushes the main-sequence wind out of the box, and $f_{\text{MS}} = 1$ for $v_{\star} = 20 \text{ km s}^{-1}$, see Fig. 7a. Conversely, the red supergiant material is distributed between the Wolf-Rayet gas and the main-sequence bow shock, and it is compressed and mixed as the blastwave propagates. Since the ring produced by the Wolf-Rayet material is out of its stellar wind bubble, the space velocity of the progenitor star matters very little, and the evolution of f_{RSG} is similar in both cases, see Fig. 7b.

The same Wolf-Rayet wind develops at early times in our supernova remnants and the ovoidal ring it carves is similar in both cases, and so is the circumstellar distribution of Wolf-Rayet material. The ring is hit by a symmetric supernova blastwave resulting from a spherical explosion, and the mixing factor f_{WR} evolves similarly in both models. The material is rapidly mixed, and eventually the Wolf-Rayet gas is distributed in small islands and clumps (Fig. 7c). The ejecta

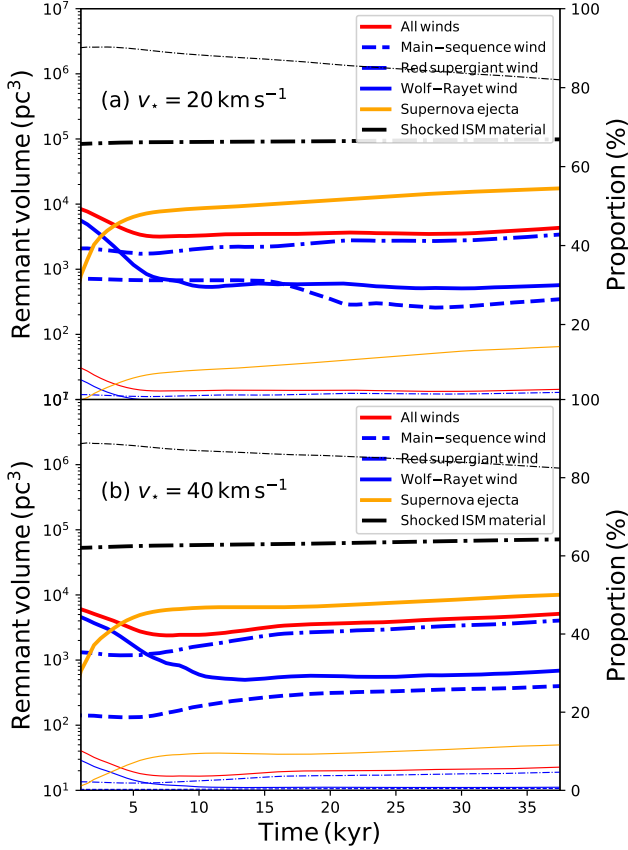


Figure 6. The volume (in pc³) occupied by the different materials inside of the supernova remnant of the slower (top) and the faster progenitor (bottom), plotted as a function of time. Each panel distinguishes between the contribution from the stellar wind (red solid line), main-sequence material (dashed blue line), red supergiant material (dotted blue line), Wolf-Rayet gas (solid blue line), supernova ejecta (solid orange line) and shocked ISM gas (dashed dotted black line). The contributions to the energy budget for each species in the simulation (thin lines, in per cent) is added to the plot.

mixing factor in the supernova remnant with velocity $v_* = 20 \text{ km s}^{-1}$ stays $f_{ej} < 0.15$ during the early 50 kyr of its evolution and evolves little over the first 20 kyr, because once the shock wave hits the circumstellar medium and is slowly reflected towards the center of the location (Fig 3), no further mixing happens. In the model with velocity $v_* = 40 \text{ km s}^{-1}$, these reflections of the blastwave are facilitated by the bow shock, which permits the shock wave to rapidly undergo further propagation to the center of the remnant, inducing more mixing of the supernova ejecta with the stellar wind (Fig 7d). At time 30 kyr the mixing factor has reached $f_{ej} = 0.4$ to further increase as the waves propagate into the remnant (Fig 3f). All in all, within a few tens of parsecs around the center of the explosion, stellar motion principally affects the mixing of supernova ejecta rather than that of the stellar winds.

A comparison of the mixing of material in supernova remnants between static and runaway progenitor stars is plotted as a yellow solid line in Fig. 7a-d. When the progenitor star does not move but evolves under the influence of the magnetic field of the ISM, the region of unshocked wind bordered by the wind/ISM contact discontinuity is elongated along the direction of the local ISM magnetic field, see (Meyer et al. 2022). The main difference between static and runaway models lies in the paucity of ($< 70\%$) mixing of main-sequence

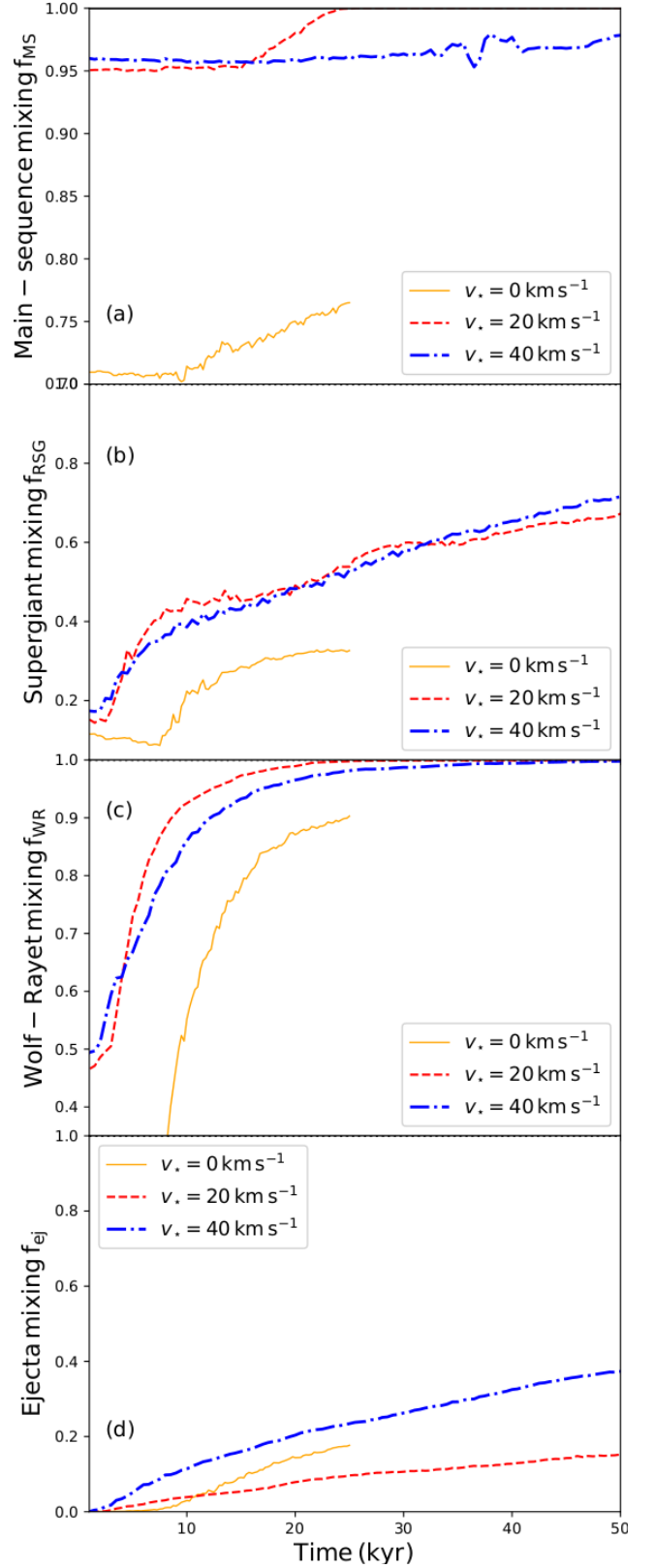


Figure 7. Mixing of the different materials in the supernova remnant during the first 50 kyr after the supernova explosion. The line colors distinguish models with stellar velocity $v_* = 0 \text{ km s}^{-1}$ (solid orange, see Meyer et al. (2022)), $v_* = 20 \text{ km s}^{-1}$ (dotted red) and $v_* = 40 \text{ km s}^{-1}$ (dotted dashed blue). The panels are for the main-sequence (a), red supergiant (b), Wolf-Rayet (c) wind material and for the supernova ejecta (d), respectively.

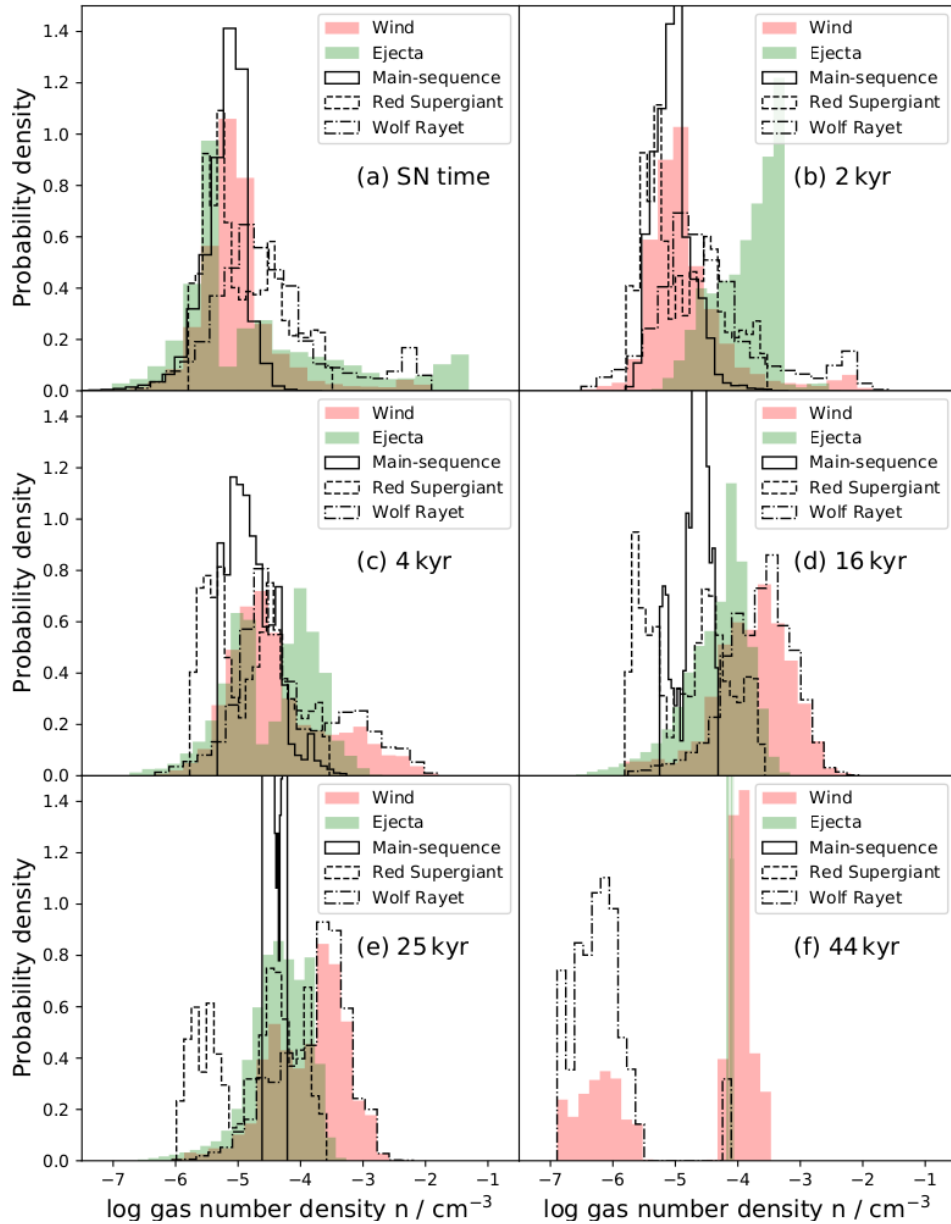


Figure 8. Probability density distribution of the gas number density (in cm^{-3}) in the supernova remnant model with $v_{\star} = 20 \text{ km s}^{-1}$, plotted for various times from the supernova explosion up to 44 kyr. The figures distinguish the different kind of materials in the supernova remnants, such as the stellar wind material (red) and the ejecta (green). The circumstellar material of the progenitor star is further divided into main-sequence (solid line), red supergiant (dotted line) and Wolf-Rayet materials (dashed line), respectively.

material for $v_{\star} = 0 \text{ km s}^{-1}$ (Fig. 7a). This also applies to the red supergiant and Wolf-Rayet wind material, see Fig. 7b,c, whose mixing efficiencies are much below that of the remnant models with runaway progenitors. The situation is different regarding the supernova ejecta, as its mixing efficiency is larger in the model with $v_{\star} = 0 \text{ km s}^{-1}$ compare to that of with $v_{\star} = 20 \text{ km s}^{-1}$ for times $> 12 \text{ kyr}$ (Fig. 7d). The reason for this is the proximity of the center of the supernova explosion with the shocked wind regions as an effect of the stretched contact discontinuity of stellar wind bubbles around static massive stars, see also [van Marle et al. \(2015\)](#).

Fig. 8 shows the volumetric distribution of the gas number density of the supernova remnant, plotted at specific times from the supernova explosion to the age of 44 kyr. The figures distinguish the stellar wind material (red) and the ejecta (green). The circumstellar

material of the progenitor star is further divided in main-sequence (solid line), red supergiant (dotted line) and Wolf-Rayet (dashed line) materials, respectively. The ejecta have a broad density distribution. It is already interacting with the stellar wind and displays a two-components distribution, while the stellar wind distribution has a single peak that is dominated by main-sequence gas. The red supergiant gas already exhibits a rather complex morphology, reflecting the complicated and knotty morphology of the circumstellar medium in which the star died (Fig. 8a). At time 2 kyr, the ejecta density distribution has evolved as a result of the interaction with the stellar wind and its expansion (Fig. 8b). At time 4 kyr both the stellar wind and the supernova ejecta distributions adopt the shape of a two-component structure. This is due to the interaction of the supernova shock wave with the Wolf-Rayet material, whose number density

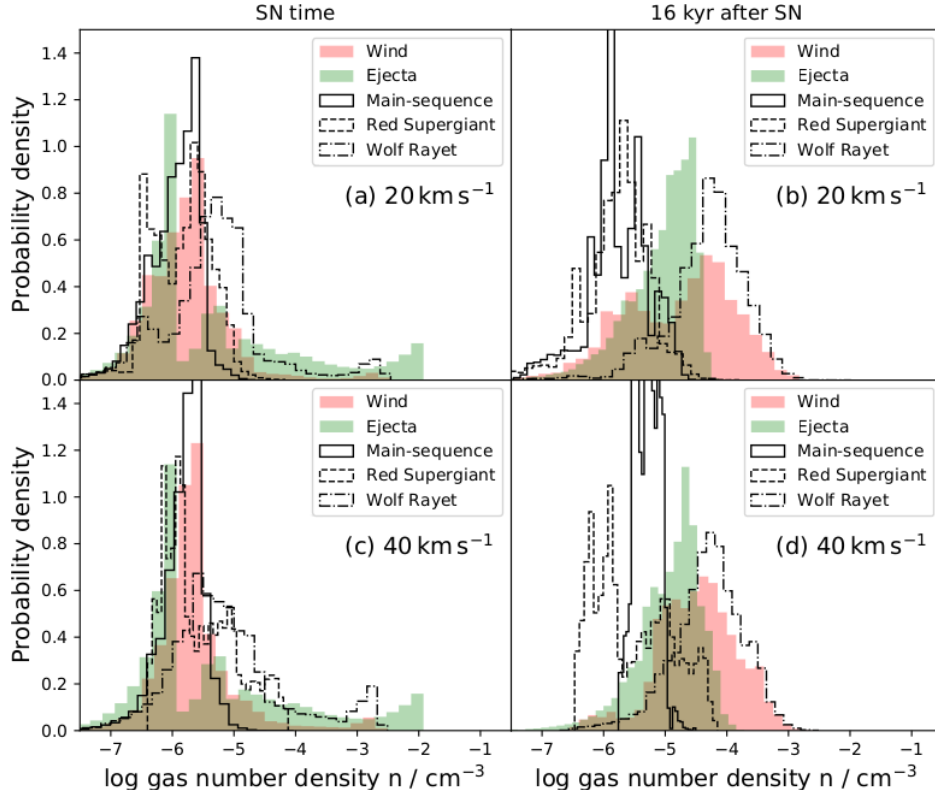


Figure 9. Comparison of the mixing of different materials in the supernova remnants for progenitor velocity $v_{\star} = 20 \text{ km s}^{-1}$ (top) and $v_{\star} = 40 \text{ km s}^{-1}$ (bottom) at the time of the supernova explosion and 16 kyr later. The figures distinguish the stellar wind material (red) and the ejecta (green). The circumstellar material of the progenitor star is further divided into main-sequence (solid line), red supergiant (dotted line) and Wolf-Rayet materials (dashed line), respectively.

increases. Similarly, the red supergiant material distribution splits into two components, and the two peaks become clearly separated when the supernova ejecta are channelled into the low-density cavity of the circumstellar medium. As the blastwave further interacts with the former bow shock, the density of shocked Wolf-Rayet gas further increases and the distribution of stellar wind gas shifts to the higher densities (Fig. 8d). At time 25 kyr the red supergiant material is efficiently mixed a pattern inside of the supernova remnant, leading to multiple components in the red supergiant wind distribution (Fig. 8e), while the Wolf-Rayet material globally increases in density. At later time (44 kyr) only some Wolf-Rayet material remains unmixed, the other kinds of stellar wind being largely melted with each other. At this time, the supernova ejecta are almost entirely dispersed into the remnant.

Fig. 9 compares the distribution of the gas density at selected times in the evolution of supernova remnants generated by a progenitor moving with velocity $v_{\star} = 20 \text{ km s}^{-1}$ (top) and $v_{\star} = 40 \text{ km s}^{-1}$ (bottom). The figures distinguish the stellar wind material (red) and the ejecta (green). The circumstellar material of the progenitor star is further divided in main-sequence, red supergiant and Wolf-Rayet materials, respectively. At the moment of the explosion, the distribution of ejecta does not depend on the progenitor speed since we used the same explosion properties for both models (Fig. 9 a,c), differences being exclusively in the distribution of the circumstellar material and shocked ISM. The stellar wind material (especially red supergiant) already exhibits a different level of mixing because a faster motion of the star induces more mixing. In the model with $v_{\star} = 20 \text{ km s}^{-1}$, this dichotomy increases at later times, when the red supergiant material enters the low-density cavity and the density distribution of

the stellar wind and the gas distribution splits into two components (Fig. 9b), whereas the distribution of Wolf-Rayet gas appears similar in both models (green histograms of Fig. 9b,d). The main difference in the density distribution is the manner the main-sequence and red supergiant gas melt into the supernova remnant with the other kind of materials, see solid and dotted lined histograms of Fig. 9b,d. The slightly more peaked distribution of supernova ejecta in the fast-moving model reflects the different reverberation properties of the supernova shock wave against the circumstellar medium (Fig. 9b,d).

4 DISCUSSION

In this last section, we recall the limitation of the models and discuss our models in the context of available observations.

4.1 Caveats of the method

Although we introduce stellar rotation and magnetised stellar wind flows in our simulations of core-collapse supernova remnants, our models are nevertheless affected by a number of limitations. The most important of them is the two-dimensional nature of the calculations, potentially impacting on the stability of the wind-ISM interaction. Three-dimensional simulations can solve this issue, however at much lower spatial resolution (Katushkina et al. 2017, 2018; Gvaramadze et al. 2018; Meyer et al. 2021c). The treatment of the ISM is also an element which can be subject to improvements, especially in terms of intrinsic turbulence and granularity of the ambient medium in which the progenitor stars evolve (Martizzi et al. 2015; Haid et al. 2016). Similarly, the interaction of the supernova shock wave with dense

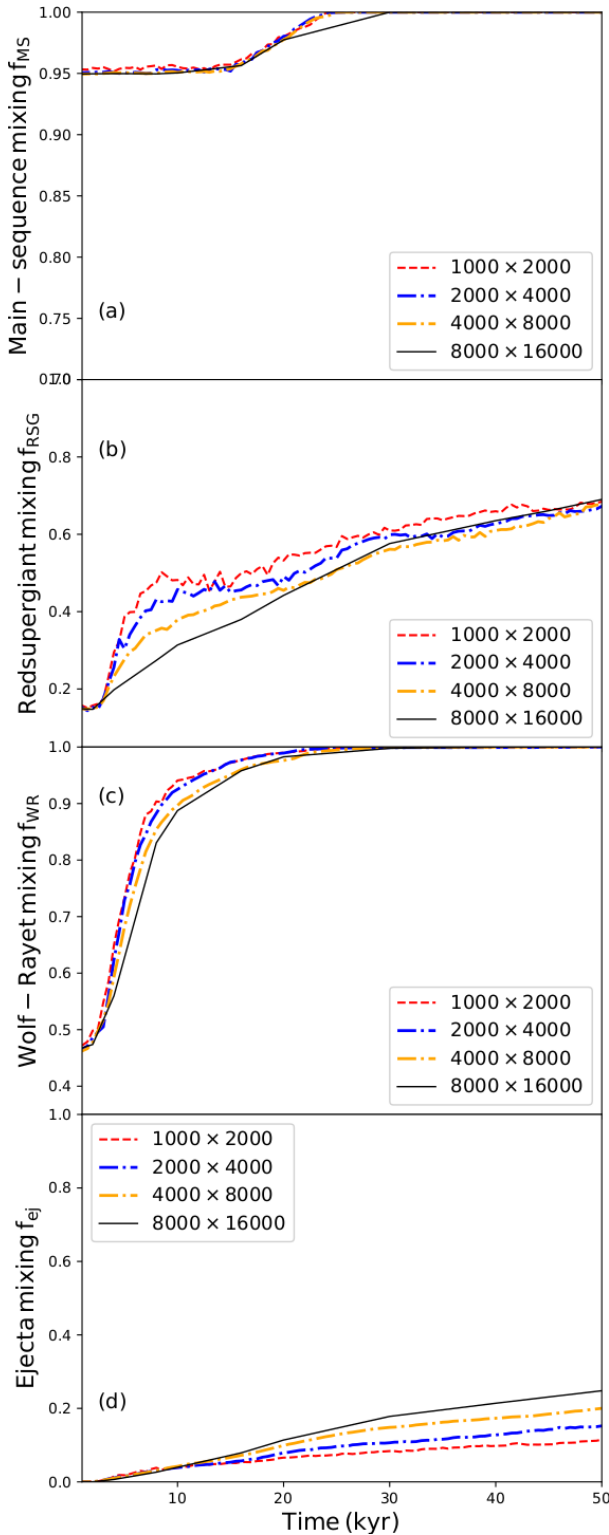


Figure 10. Effect of spatial resolution on the mixing of the different materials in the supernova remnants, plotted as a function of time (in kyr) for the models with stellar velocity $v_{\star} = 20 \text{ km s}^{-1}$. The panels show the mixing efficiency in simulations performed with spatial resolutions 1000×2000 (dashed red line), 2000×4000 (dotted dashed blue line), 4000×8000 (solid orange line) and 8000×16000 (solid black line). The figures plot the evolution of the mixing efficiency during the early 50 kyr after the supernova explosion for the main-sequence (a), red supergiant (b), Wolf-Rayet (c) stellar winds and for the supernova ejecta (d), respectively.

molecular regions (McKee & Cowie 1975; van Dishoeck et al. 1993) or low-density parts (Arias et al. 2019) of the ISM which might modify the propagation of the forward shock of the expanding supernova should also be investigated in future studies as this may be a key factor in the shaping of middle-age supernova remnants (Ferreira & de Jager 2008; Rathjen et al. 2021). Last, several physical mechanisms must be incorporated into the simulations of our study, such as anisotropic heat conduction (Bedogni & D’Ercole 1988; Velázquez et al. 2004; Orlando et al. 2005; Vieser & Hensler 2007; Balsara et al. 2008a,b) or an explicit treatment of the photoionization of the progenitor star in order to simulate the degree of ionization of the gas in the remnant (see e.g. García-Segura et al. 1999; van Marle et al. 2004; Arthur & Hoare 2006; Toalá & Arthur 2011).

4.2 Effects of spatial resolution

Fig. 10 repeats the analysis presented in Fig. 7 by investigating the effect of spatial resolution on the time evolution of the mixing of the different materials in the supernova remnant models with stellar velocity $v_{\star} = 20 \text{ km s}^{-1}$. The panels show the mixing efficiency in simulations performed with spatial resolutions 1000×2000 (dashed red line), 2000×4000 (dotted dashed blue line), 4000×8000 (dashed dotted orange line) and 8000×16000 (solid black line). The tracers in the simulation are used to separate the mixing efficiency during the early 50 kyr after the supernova explosion for the main-sequence (a), red supergiant (b), Wolf-Rayet (c) stellar winds and for the supernova ejecta (d), respectively. No notable differences in terms of mixing efficiency of the main-sequence material happens, especially because most of this kind of gas has left the computational domain at times $\geq 25 \text{ kyr}$. Note that because of the definition that we adopted, the mixing factor equals to unity once all the material has left the computational domain (Fig. 10a). The mixing of the red supergiant material is the most sensitive to spatial resolution. The variability of the mixing factor diminishes with the increasing spatial resolution, and its value is slightly overestimated when the resolution is too coarse (Fig. 10b). The models show that it has not yet converged, except at longer times $\geq 45 \text{ kyr}$, and that even higher-resolution simulations are needed to carefully track the mixing of the dusty supergiant material into supernova remnants. Inversely, the Wolf-Rayet gas mixes quickly into the remnants, and has already converged in our low-resolution models (Fig. 10c). The ejecta mixing behaves differently: the mixing efficiency increases by a factor of ≈ 2 when the resolution is multiplied by a factor of 4 (Fig. 10d). High-resolution is therefore a key ingredient of core-collapse supernova mixing modelling (Orlando et al. 2019).

4.3 Spatial distribution of the mixed material

Fig. 11 displays the distribution of mixed materials in the supernova remnant generated by a progenitor moving with velocities 20 km s^{-1} (left panels) and 40 km s^{-1} (right panels), shown at times 8 kyr (top panels) and 80 kyr (bottom panels). The figures plot the value of the quantity Q_{RSG} representing the proportion of red supergiant (left part of the panels) and the quantity Q_{WR} representing the proportion of Wolf-Rayet (right part of the panels) materials, respectively. The blue contours of the passive scalar field Q_{EJ} indicate a 10 per cent contribution of ejecta in number density. At times 8 kyr there are few differences between the models. The enriched gases are distributed as a ring surrounding the expanding supernova blastwave that is interacting with the pre-supernova circumstellar medium (Fig. 11a,b). The low-density cavity of the model with 20 km s^{-1} mostly contains red

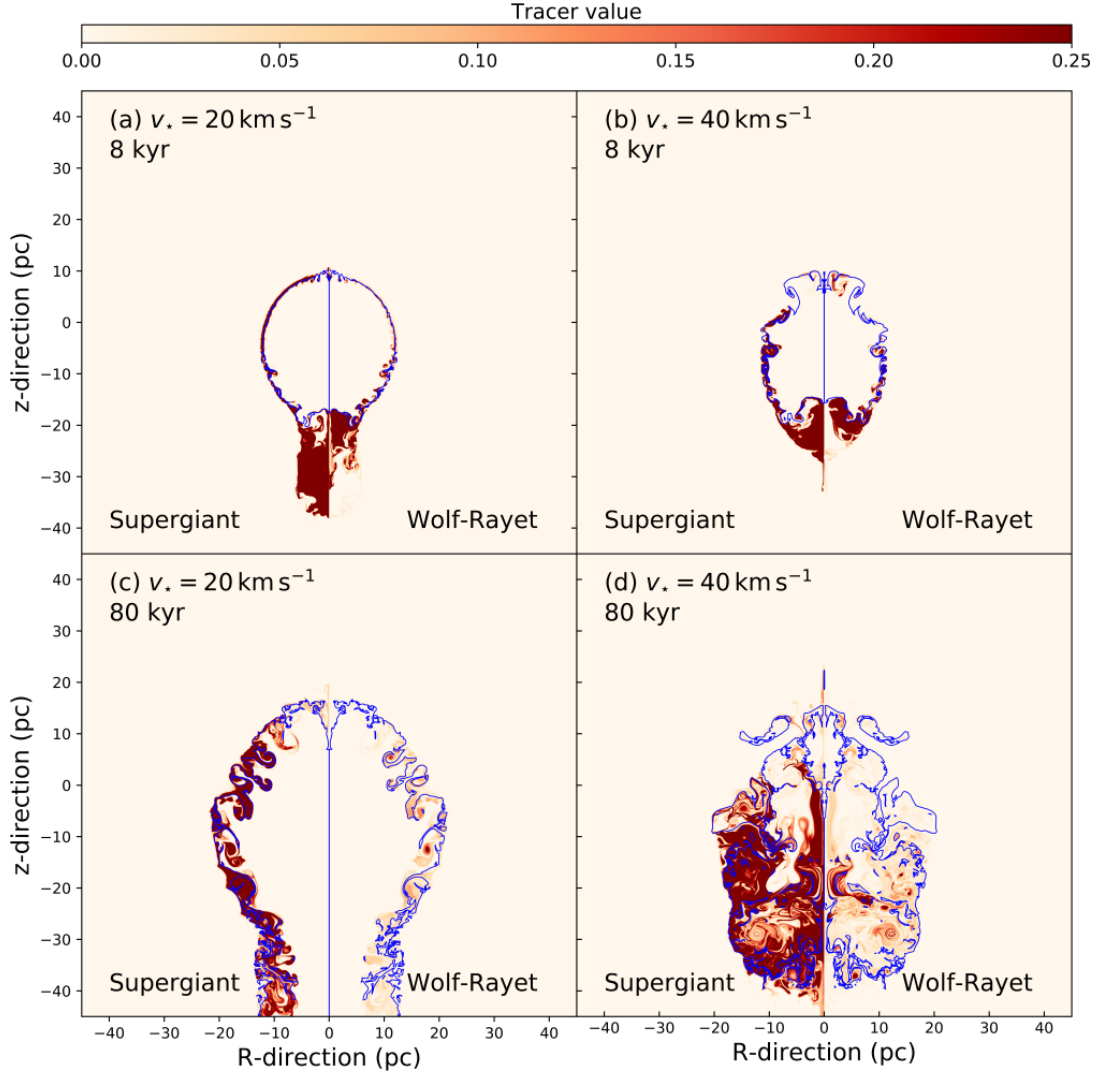


Figure 11. Mixing of material in the supernova remnants generated by a progenitor moving with velocity 20 km s^{-1} (left) and 40 km s^{-1} (right), shown at times 8 kyr (top) and 80 kyr (bottom). The figures plot the value of the quantity Q_{RSG} representing the proportion of red supergiant (left part of the panels) and the quantity Q_{WR} representing the proportion of Wolf-Rayet (right part of the panels) materials, respectively. The blue contours of the passive scalar field Q_{EJ} indicate a 10 per cent contribution of ejecta in number density.

supergiant material channelled into it (Fig. 11a). When the supernova remnant is much older (80 kyr), the manner the blastwave reflected towards the center of the explosion also governs the distribution of the stellar winds. Massive bow shocks have stopped the blastwave after its first reverberation (Meyer et al. 2015, 2021b), and both the red supergiant and Wolf-Rayet material are located around the location where the supernova shock wave interacted with the circumstellar medium, producing a Cygnus-loop-like region filled with ejecta and post-main-sequence materials (Fig. 11c). In the other model with 40 km s^{-1} , the red supergiant gas fills the lower ($z < 0$) region of the supernova remnant, in which clumps of Wolf-Rayet-rich gas are scattered. This is a major difference between remnants from slow- and fast-moving progenitors, which has observable consequences.

4.4 Motivation of the choice of an initial $35 M_{\odot}$ progenitor

This work constitutes the method paper of a series of studies devoted to the comprehensive modelling of supernova remnants of static and runaway massive stars. A single, non-rotating model has already been

published, presenting thermal and non-thermal emission maps of the transient rectangular-like supernova remnant generated when a supernova blastwave interacts with the elongated termination shock of a stellar wind bubble forming around a massive star located in a uniformly magnetised environment. It underlined how this mechanism may participate in the shaping of the rectangular supernova remnant Puppis A (Meyer et al. 2022). The choice of a $35 M_{\odot}$ progenitor had been motivated by conclusions from observations of Puppis A (Paron et al. 2008), although alternative scenarios with lower-mass scenarios are currently considered (Velázquez et al. 2023). Our work continues this numerical effort by exploring the bulk motion of the same Wolf-Rayet-evolving progenitor. The zero-age main-sequence rotation rate of the massive star used to simulate our supernova remnants is taken to 10% of its break-up velocity. It is necessary to include rotation in the simulations otherwise the toroidal component of the stellar magnetic field vanishes and only the insignificantly weak radial component will remain. This will let the unshocked supernova ejecta unmagnetised and make the exercise of Fig. 4 impossible with respect to the magnetic energy. Further models will be performed in

the future in order to continue investigating how the surroundings of defunct high-mass stars look like, e.g. by considering different initial progenitor masses and/or environments. A global picture regarding the mixing of enriched materials via core-collapse supernova remnants will hence emerge.

This collection of remnants will serve as a basis for the detailed study of several potential individual targets. Amongst others, one can mention a few supernova remnants of constrained initial mass consistent with a formation scenario involving a Wolf-Rayet progenitor: Kes 73, G292.2-0.5, G349.7+0.2, G292.0+1.8, Kes 79, Kes 17, in the Milky Way, N132D in the Large Magellanic Cloud or 1E0102.2-7219 in the Small Magellanic Cloud. Note that our precedent work (Meyer et al. 2021b) has established that supernova progenitors evolving through a Wolf-Rayet phase can produce bilateral and the shell-type remnants such as G296.5+10.0 and CTB109, respectively, at least as seen in the radio waveband by non-thermal emission. Such Galactic and extragalactic objects which are the perfect targets for tailoring our results to specific core-collapse supernova remnants. Last, let also note that the *Cherenkov Telescope Array* (CTA) will help in discovering new core-collapse supernova remnants to which understanding will require numerical models.

5 CONCLUSION

This paper investigates the evolution of young to middle-age core-collapse supernova remnants generated by a $35 M_{\odot}$ massive runaway star with particular emphasis on the mixing of materials. Our 2.5D magneto-hydrodynamical numerical simulations account for the rotation (Ekström et al. 2012) and magnetisation (Meyer et al. 2021c; Baalmann et al. 2020, 2021) of the progenitor star that is moving through the warm, uniform, magnetised phase of the interstellar medium of the Milky Way. A system of passive scalar tracers permits us to follow the advection of the different kind of wind materials throughout the pre-supernova evolution of the progenitor. The simulations are conducted in the fashion of the precedent papers of this series, by first modelling the detailed circumstellar medium of the progenitor star at the pre-supernova time, and by releasing into it a separately calculated solution for the ejecta-wind that is simulated up to 100 kyr, see (Meyer et al. 2015, 2020a, 2021b). The high-resolution calculations are performed using the *PLUTO* code (Mignone et al. 2007, 2012; Vaidya et al. 2018) that has been validated for circumstellar medium and supernova remnants studies (Meyer et al. 2014, 2017).

It is found that the manner the stellar winds associated to the various evolutionary phases of the progenitor, as well as the supernova ejecta, distribute into the supernova remnant differs greatly depending on the bulk motion of the star, the level of wind mixing increasing with it, i.e. faster-moving progenitors generate older remnants hosting more complex, dense filamentary internal patterns of mixed species, where wind mixes less but ejecta does it better. Very little main-sequence material ($\leq 5\%$) is present in the remnants, as it is channelled into the tubular low-density cavity of wind produced by the progenitor's stellar motion. The red supergiant material is the least mixed species, while the Wolf-Rayet gas efficiently mixes in the early 20 kyr after the explosion.

Our results show that the spatial distribution of the post-main-sequence stellar winds depends on the progenitor's spatial motion. At later times after the supernova explosion (> 40 kyr), the reflection of the supernova blastwave spreads wind material to the interior of the remnant nebula, distributing Wolf-Rayet clumps inside of it, if the progenitor's motion is important ($v_{\star} = 40 \text{ km s}^{-1}$). The enriched

stellar wind material remains in the region of the pre-supernova circumstellar medium for slower progenitors ($v_{\star} = 20 \text{ km s}^{-1}$). Interestingly, the mixing efficiency of ejecta is less important in the context of runaway progenitors than in the case of a massive star (Meyer et al. 2022). The spatial resolution is very important in the numerical study of mixing processes into core-collapse supernova remnants, as a low resolution tends to overestimate that of the red supergiant and Wolf-Rayet stellar winds and underestimates that of the supernova ejecta. Indeed, the regions filled by the winds turned to be isolate islands located around the shell made of the circumstellar medium shocked by the blastwave, where the material is both sub-sonic and supersonic. Such work should be extended to the stellar clusters made of multiple massive stars (Badmaev et al. 2022).

ACKNOWLEDGEMENTS

The authors acknowledge the North-German Supercomputing Alliance (HLRN) for providing HPC resources that have contributed to the research results reported in this paper. M. Petrov acknowledges the Max Planck Computing and Data Facility (MPCDF) for providing data storage resources and HPC resources which contributed to test and optimise the *PLUTO* code.

DATA AVAILABILITY

This research made use of the *PLUTO* code developed at the University of Torino by A. Mignone (<http://plutocode.ph.unito.it/>). The figures have been produced using the Matplotlib plotting library for the Python programming language (<https://matplotlib.org/>). The data underlying this article will be shared on reasonable request to the corresponding author.

REFERENCES

- Ahmadi A., et al., 2018, *A&A*, **618**, A46
- Aloy M. Á., Obergaulinger M., 2021, *MNRAS*, **500**, 4365
- Arias M., et al., 2019, *A&A*, **622**, A6
- Arnaud K. A., 1996, in Jacoby G. H., Barnes J., eds, *Astronomical Society of the Pacific Conference Series Vol. 101, Astronomical Data Analysis Software and Systems V*. p. 17
- Arthur S. J., Hoare M. G., 2006, *ApJS*, **165**, 283
- Asplund M., Grevesse N., Sauval A. J., Scott P., 2009, *ARA&A*, **47**, 481
- Baalmann L. R., Scherer K., Fichtner H., Kleimann J., Bomans D. J., Weis K., 2020, *A&A*, **634**, A67
- Baalmann L. R., Scherer K., Kleimann J., Fichtner H., Bomans D. J., Weis K., 2021, *A&A*, **650**, A36
- Badmaev D. V., Bykov A. M., Kalyashova M. E., 2022, *MNRAS*, **517**, 2818
- Balsara D. S., Tilley D. A., Howk J. C., 2008a, *MNRAS*, **386**, 627
- Balsara D. S., Bendinelli A. J., Tilley D. A., Massari A. R., Howk J. C., 2008b, *MNRAS*, **386**, 642
- Bandiera R., Bucciantini N., Martín J., Olmi B., Torres D. F., 2023, *MNRAS*, **521**, 1000
- Baranov V. B., Krasnobaev K. V., Kulikovskii A. G., 1971, *Soviet Physics Doklady*, **15**, 791
- Bedogni R., D'Ercole A., 1988, *A&A*, **190**, 320
- Benaglia P., Romero G. E., Martí J., Peri C. S., Araudo A. T., 2010, *A&A*, **517**, L10
- Blaauw A., 1961, *Bull. Astron. Inst. Netherlands*, **15**, 265
- Blondin J. M., Lundqvist P., Chevalier R. A., 1996, *ApJ*, **472**, 257
- Brighenti F., D'Ercole A., 1995a, *MNRAS*, **273**, 443
- Brighenti F., D'Ercole A., 1995b, *MNRAS*, **277**, 53
- Broersen S., Chiotellis A., Vink J., Bamba A., 2014, *MNRAS*, **441**, 3040
- Brott I., et al., 2011a, *A&A*, **530**, A115

- Brott I., et al., 2011b, *A&A*, **530**, A116
- Castro N., et al., 2015, *A&A*, **581**, A81
- Castro N., et al., 2017, *A&A*, **597**, L6
- Chevalier R. A., 1982, *ApJ*, **258**, 790
- Chevalier R. A., Liang E. P., 1989, *ApJ*, **344**, 332
- Chevalier R. A., Luo D., 1994, *ApJ*, **421**, 225
- Chiotellis A., Schure K. M., Vink J., 2012, *A&A*, **537**, A139
- Chiotellis A., Kosenko D., Schure K. M., Vink J., Kaastra J. S., 2013, *MNRAS*, **435**, 1659
- Chiotellis A., Boumis P., Derlopa S., Steffen W., 2019, arXiv e-prints, p. [arXiv:1909.08947](https://arxiv.org/abs/1909.08947)
- Chiotellis A., Boumis P., Spetsieri Z. T., 2020, *Galaxies*, **8**, 38
- Chiotellis A., Boumis P., Spetsieri Z. T., 2021, *MNRAS*, **502**, 176
- Chita S. M., Langer N., van Marle A. J., García-Segura G., Heger A., 2008, *A&A*, **488**, L37
- Comerón F., Kaper L., 1998, *A&A*, **338**, 273
- Crowther P. A., 2007, *ARA&A*, **45**, 177
- Das S., Brose R., Meyer D. M. A., Pohl M., Sushch I., Plotko P., 2022, *A&A*, **661**, A128
- Davies B., 2017, *Philosophical Transactions of the Royal Society of London Series A*, **375**, 20160270
- De Becker M., del Valle M. V., Romero G. E., Peri C. S., Benaglia P., 2017, *MNRAS*, **471**, 4452
- Derlopa S., Boumis P., Chiotellis A., Steffen W., Akas S., 2019, arXiv e-prints, p. [arXiv:1909.06131](https://arxiv.org/abs/1909.06131)
- Dwarkadas V. V., 2005, *ApJ*, **630**, 892
- Dwarkadas V. V., 2007, *ApJ*, **667**, 226
- Ekström S., et al., 2012, *A&A*, **537**, A146
- Eldridge J. J., Genet F., Daigne F., Mochkovitch R., 2006, *MNRAS*, **367**, 186
- Fang J., Yu H., Zhang L., 2017, *MNRAS*, **464**, 940
- Ferreira S. E. S., de Jager O. C., 2008, *A&A*, **478**, 17
- Finn K., Bianco F. B., Modjaz M., Liu Y.-Q., Rest A., 2016, *ApJ*, **830**, 73
- Fossati L., et al., 2015, *A&A*, **574**, A20
- Freyer T., Hensler G., Yorke H. W., 2006, *ApJ*, **638**, 262
- Gabler M., Wongwathanarat A., Janka H.-T., 2021, *MNRAS*, **502**, 3264
- García-Segura G., Mac Low M.-M., Langer N., 1996a, *A&A*, **305**, 229
- García-Segura G., Langer N., Mac Low M.-M., 1996b, *A&A*, **316**, 133
- García-Segura G., Langer N., Różyczka M., Franco J., 1999, *ApJ*, **517**, 767
- García-Segura G., Ricker P. M., Taam R. E., 2018, *ApJ*, **860**, 19
- García-Segura G., Taam R. E., Ricker P. M., 2020, *ApJ*, **893**, 150
- Gies D. R., 1987, *ApJS*, **64**, 545
- Green S., Mackey J., Haworth T. J., Gvaramadze V. V., Duffy P., 2019, *A&A*, **625**, A4
- Groh J. H., Meynet G., Ekström S., Georgy C., 2014, *A&A*, **564**, A30
- Gull T. R., Sofia S., 1979, *ApJ*, **230**, 782
- Gvaramadze V. V., 2006, *A&A*, **454**, 239
- Gvaramadze V. V., Weidner C., Kroupa P., Pflamm-Altenburg J., 2012, *MNRAS*, **424**, 3037
- Gvaramadze V. V., Alexashov D. B., Katushkina O. A., Kniazev A. Y., 2018, *MNRAS*, **474**, 4421
- Haid S., Walch S., Naab T., Seifried D., Mackey J., Gatto A., 2016, *MNRAS*, **460**, 2962
- Hamann W. R., 1992, in Heber U., Jeffery C. S., eds., , Vol. 401, The Atmospheres of Early-Type Stars. p. 87
- Harten A., Lax P. D., van Leer B., 1983, *SIAM Review*, **25**, 35
- Herbst K., et al., 2020, *ApJ*, **897**, L27
- Herbst K., et al., 2022, *Space Sci. Rev.*, **218**, 29
- Holland-Ashford T., Lopez L. A., Auchettl K., 2020, *ApJ*, **889**, 144
- Hummer D. G., 1994, *MNRAS*, **268**, 109
- Ilee J. D., Cyganowski C. J., Nazari P., Hunter T. R., Brogan C. L., Forgan D. H., Zhang Q., 2016, *MNRAS*, **462**, 4386
- Jardine R., Powell J., Müller B., 2022, *MNRAS*, **510**, 5535
- Johnston K. G., et al., 2015, *ApJ*, **813**, L19
- Kaper L., van Loon J. T., Augusteijn T., Goudfrooij P., Patat F., Waters L. B. F. M., Zijlstra A. A., 1997, *ApJ*, **475**, L37
- Katsuda S., Takiwaki T., Tominaga N., Moriya T. J., Nakamura K., 2018, *ApJ*, **863**, 127
- Katushkina O. A., Alexashov D. B., Izmodenov V. V., Gvaramadze V. V., 2017, *MNRAS*, **465**, 1573
- Katushkina O. A., Alexashov D. B., Gvaramadze V. V., Izmodenov V. V., 2018, *MNRAS*, **473**, 1576
- Kervella P., et al., 2018, *A&A*, **609**, A67
- Kifonidis K., Plewa T., Scheck L., Janka H. T., Müller E., 2006, *A&A*, **453**, 661
- Kobulnicky H. A., et al., 2016, *ApJS*, **227**, 18
- Kobulnicky H. A., Schurhammer D. P., Baldwin D. J., Chick W. T., Dixon D. M., Lee D., Povich M. S., 2017, *AJ*, **154**, 201
- Kroupa P., 2001, *MNRAS*, **322**, 231
- Langer N., 2012, *ARA&A*, **50**, 107
- Levesque E. M., 2010, *New Astron. Rev.*, **54**, 1
- Mackey J., Mohamed S., Neilson H. R., Langer N., Meyer D. M.-A., 2012, *ApJ*, **751**, L10
- Maeder A., Meynet G., 2000, *ARA&A*, **38**, 143
- Martizzi D., Faucher-Giguère C.-A., Quataert E., 2015, *MNRAS*, **450**, 504
- McKee C. F., Cowie L. L., 1975, *ApJ*, **195**, 715
- Meyer D. M. A., 2021, *MNRAS*, **507**, 4697
- Meyer D. M. A., Meliani Z., 2022, *MNRAS*, **515**, L29
- Meyer D. M.-A., Mackey J., Langer N., Gvaramadze V. V., Mignone A., Izzard R. G., Kaper L., 2014, *MNRAS*, **444**, 2754
- Meyer D. M.-A., Langer N., Mackey J., Velázquez P. F., Gusdorf A., 2015, *MNRAS*, **450**, 3080
- Meyer D. M.-A., van Marle A.-J., Kuiper R., Kley W., 2016, *MNRAS*, **459**, 1146
- Meyer D. M.-A., Vorobyov E. I., Kuiper R., Kley W., 2017, *MNRAS*, **464**, L90
- Meyer D. M. A., Vorobyov E. I., Elbakyan V. G., Stecklum B., Eislöffel J., Sobolev A. M., 2019, *MNRAS*
- Meyer D. M. A., Petrov M., Pohl M., 2020a, *MNRAS*, **493**, 3548
- Meyer D. M. A., Oskinova L. M., Pohl M., Petrov M., 2020b, *MNRAS*, **496**, 3906
- Meyer D. M. A., Vorobyov E. I., Elbakyan V. G., Eislöffel J., Sobolev A. M., Stöhr M., 2021a, *MNRAS*, **500**, 4448
- Meyer D. M. A., Pohl M., Petrov M., Oskinova L., 2021b, *MNRAS*, **502**, 5340
- Meyer D. M. A., Mignone A., Petrov M., Scherer K., Velázquez P. F., Boumis P., 2021c, *MNRAS*, **506**, 5170
- Meyer D. M. A., et al., 2022, *MNRAS*, **515**, 594
- Mignone A., Bodo G., Massaglia S., Matsakos T., Tesileanu O., Zanni C., Ferrari A., 2007, *ApJS*, **170**, 228
- Mignone A., Zanni C., Tzeferacos P., van Straalen B., Colella P., Bodo G., 2012, *ApJS*, **198**, 7
- Moffat A. F. J., Marchenko S. V., Seggewiss W., van der Hucht et al. K. A. e. a., 1998, *A&A*, **331**, 949
- Müller B., Janka H. T., 2015, *MNRAS*, **448**, 2141
- Müller E., Janka H. T., Wongwathanarat A., 2012, *A&A*, **537**, A63
- Olmi B., Bucciantini N., 2019, *MNRAS*, **490**, 3608
- Olmi B., Bucciantini N., 2023, arXiv e-prints, p. [arXiv:2301.12903](https://arxiv.org/abs/2301.12903)
- Orlando S., Peres G., Reale F., Bocchino F., Rosner R., Plewa T., Siegel A., 2005, *A&A*, **444**, 505
- Orlando S., et al., 2019, *A&A*, **622**, A73
- Orlando S., et al., 2020, *A&A*, **636**, A22
- Osterbrock D. E., Bochkarev N. G., 1989, *Soviet Ast.*, **33**, 694
- Parker E. N., 1958, *ApJ*, **128**, 664
- Paron S., Dubner G., Reynoso E., Rubio M., 2008, *A&A*, **480**, 439
- Peri C. S., Benaglia P., Brookes D. P., Stevens I. R., Isequilla N. L., 2012, *A&A*, **538**, A108
- Peri C. S., Benaglia P., Isequilla N. L., 2015, *A&A*, **578**, A45
- Pogorelov N. V., Matsuda T., 2000, *A&A*, **354**, 697
- Pogorelov N. V., Semenov A. Y., 1997, *A&A*, **321**, 330
- Powell K. G., 1997, An Approximate Riemann Solver for Magneto-hydrodynamics. Springer Berlin Heidelberg, Berlin, Heidelberg, pp 570–583, doi:10.1007/978-3-642-60543-7_23, https://doi.org/10.1007/978-3-642-60543-7_23
- Przybilla N., et al., 2016, *A&A*, **587**, A7
- Raga A. C., Mellema G., Lundqvist P., 1997, *ApJS*, **109**, 517

Rathjen T.-E., et al., 2021, *MNRAS*, **504**, 1039
 Rozyczka M., Franco J., 1996, *ApJ*, **469**, L127
 Salpeter E. E., 1955, *ApJ*, **121**, 161
 Sana H., et al., 2012, *Science*, **337**, 444
 Scherer K., Baalmann L. R., Fichtner H., Kleimann J., Bomans D. J., Weis K., Ferreira S. E. S., Herbst K., 2020, *MNRAS*, **493**, 4172
 Shu F. H., 1992, The physics of astrophysics. Volume II: Gas dynamics.
 Smartt S. J., 2009, *ARA&A*, **47**, 63
 Smith N., 2014, *ARA&A*, **52**, 487
 Szécsi D., Agrawal P., Wünsch R., Langer N., 2022, *A&A*, **658**, A125
 Telezhinsky I., Dwarkadas V. V., Pohl M., 2012a, *Astroparticle Physics*, **35**, 300
 Telezhinsky I., Dwarkadas V. V., Pohl M., 2012b, *A&A*, **541**, A153
 Telezhinsky I., Dwarkadas V. V., Pohl M., 2013, *A&A*, **552**, A102
 Tenorio-Tagle G., Bodenheimer P., Franco J., Rozyczka M., 1990, *MNRAS*, **244**, 563
 Tenorio-Tagle G., Rozyczka M., Franco J., Bodenheimer P., 1991, *MNRAS*, **251**, 318
 Toalá J. A., Arthur S. J., 2011, *ApJ*, **737**, 100
 Toledo-Roy J. C., Esquivel A., Velázquez P. F., Reynoso E. M., 2014, *MNRAS*, **442**, 229
 Truelove J. K., McKee C. F., 1999, *ApJS*, **120**, 299
 Tutone A., et al., 2020, *A&A*, **642**, A67
 Uchida H., Tsunemi H., Katsuda S., Kimura M., Kosugi H., 2009, *PASJ*, **61**, 301
 Underhill A. B., 1968, *ARA&A*, **6**, 39
 Vaidya B., Mignone A., Bodo G., Rossi P., Massaglia S., 2018, *ApJ*, **865**, 144
 Velázquez P. F., Martinell J. J., Raga A. C., Giacani E. B., 2004, *ApJ*, **601**, 885
 Velázquez P. F., Vigh C. D., Reynoso E. M., Gómez D. O., Schneider E. M., 2006, *ApJ*, **649**, 779
 Velázquez P. F., Meyer D. M. A., Chiotellis A., Cruz-Álvarez A. E., Schneider E. M., Toledo-Roy J. C., Reynoso E. M., Esquivel A., 2023, *MNRAS*, **519**, 5358
 Vieser W., Hensler G., 2007, *A&A*, **472**, 141
 Vigh C. D., Velázquez P. F., Gómez D. O., Reynoso E. M., Esquivel A., Matias Schneider E., 2011, *ApJ*, **727**, 32
 Vink J. S., de Koter A., Lamers H. J. G. L. M., 2000, *A&A*, **362**, 295
 Vlemmings W. H. T., Diamond P. J., van Langevelde H. J., 2002, *A&A*, **394**, 589
 Vlemmings W. H. T., van Langevelde H. J., Diamond P. J., 2005, *A&A*, **434**, 1029
 Vorobyov E. I., 2009, *ApJ*, **704**, 715
 Vorobyov E. I., 2010, *ApJ*, **723**, 1294
 Vorobyov E. I., Basu S., 2006, *ApJ*, **650**, 956
 Weaver R., McCray R., Castor J., Shapiro P., Moore R., 1977, *ApJ*, **218**, 377
 Weber E. J., Davis Leverett J., 1967, *ApJ*, **148**, 217
 Weiler K. W., Sramek R. A., 1988, *ARA&A*, **26**, 295
 Whalen D., van Veelen B., O’Shea B. W., Norman M. L., 2008, *ApJ*, **682**, 49
 Wiersma R. P. C., Schaye J., Smith B. D., 2009, *MNRAS*, **393**, 99
 Wilkin F. P., 1996, *ApJ*, **459**, L31
 Woosley S. E., Weaver T. A., 1986, *ARA&A*, **24**, 205
 Yusef-Zadeh F., Wardle M., Rho J., Sakano M., 2003, *ApJ*, **585**, 319
 Zavlin V. E., Pavlov G. G., Trumper J., 1998, *A&A*, **331**, 821
 del Valle M. V., Romero G. E., De Becker M., 2013, *A&A*, **550**, A112
 van Dishoeck E. F., Jansen D. J., Phillips T. G., 1993, *A&A*, **279**, 541
 van Marle A. J., Langer N., García-Segura G., 2004, in G. García-Segura, G. Tenorio-Tagle, J. Franco, & H. W. Yorke ed., *Revista Mexicana de Astronomía y Astrofísica Conference Series Vol. 22*, *Revista Mexicana de Astronomía y Astrofísica Conference Series*. pp 136–139
 van Marle A. J., Langer N., García-Segura G., 2005, *A&A*, **444**, 837
 van Marle A. J., Langer N., García-Segura G., 2007, *A&A*, **469**, 941
 van Marle A. J., Smith N., Owocki S. P., van Veelen B., 2010, *MNRAS*, **407**, 2305
 van Marle A. J., Meliani Z., Keppens R., Decin L., 2011, *ApJ*, **734**, L26
 van Marle A. J., Decin L., Meliani Z., 2014, *A&A*, **561**, A152
 van Marle A. J., Meliani Z., Marcowith A., 2015, *A&A*, **584**, A49

van Veelen B., Langer N., Vink J., García-Segura G., van Marle A. J., 2009, *A&A*, **503**, 495

This paper has been typeset from a \LaTeX file prepared by the author.